



INFLUENCE OF ASSEMBLY GAP AND SHIMS ON THE STRAIN AND STRESS OF BOLTED COMPOSITE-ALUMINUM STRUCTURES

Cephas Yaw Attahu^{1,2} and Luling An^{1,2}

¹Department of Aerospace Manufacturing Engineering, Nanjing University of Aeronautics and Astronautics, Nanjing, China

²Jiangsu Key Laboratory of Precision and Micro-Manufacturing Technology, Nanjing, China

E-Mail: cyattahu@gmail.com

ABSTRACT

Airframe structures are assembled using mechanical fasteners (bolts) and in assembling these structures, misalignments do occur due to parts' geometrical imperfections. This leads to the development of assembly gaps which are detrimental to the structural integrity of the assembled structure when left unshimmed. This paper seeks to investigate the influence of the assembly gap and shims on the strains and stresses of a bolted composite-aluminum structure using a non-linear three-dimensional (3-D) structural solid elements on an assembled compressive open-hole model of a carbon fiber-reinforced polymer (CFRP) - aluminum alloy (AA). The model was generated with the commercial finite element (FE) software package, ABAQUS /Standard and the assembled 3-D FE model simulated, as well as the specimen for the experimental testing, consisted of a CFRP substrate, AA 7075-T651 substrate, liquid shim (Hysol EA 9394), solid peelable fiberglass shim, a titanium fastener and washer. In distinction to previous investigations, the influence of assembly gap and shims (liquid shim and solid peelable fiberglass shim) were investigated by both numerical simulations and experimental work. To validate the results, six (6) strain gages were bonded at various locations on the surface of the composite plate and the strain values recorded. The experimental results corresponded very well with that of numerical results. The simulated model and the test specimen conformed to the composite bearing response and the open-hole tensile strength test standards of American Society for Testing and Materials, D5961/D5961M-13 and D5766/D5766M-07 respectively which is the standard test configurations for this kind of study. It has been found that: (1) the shimming procedure as agreed upon by the aerospace industry for the resolution of assembly gaps in bolted joints for composite materials is same as that for a composite-aluminum structure; (2) there were large stress and strain concentrations generated between the assembly gaps for the unshimmed models :-increasing assembly gaps resulted in an increasing stresses and strains, and (3) the assembly gap and shims significantly influenced the strains and stresses:-the shims decreased the stress and strain concentrations generated between the assembly gap.

Keywords: aircraft assembly gap, shim, bolted structures, composite-aluminum, strain, stress.

INTRODUCTION

Stress and strain concentrations in composite structures, in particular, are problematic because it leads to strength deteriorations, damage accumulations and eventually to failure. This paper seeks to establish how the assembly gap and shim get affected by stresses and strains, and the need to shim these assembly gaps.

Aluminum alloys have been an important aerospace structural material in the development of weight-efficient airframes for a long time. The development of aircraft capable of flying at high speeds and high altitudes would have been difficult without the use of high-strength aluminum alloys in major airframe components such as the fuselage and wings. Aluminum alloys are likely to remain an important structural material despite the growing use of composites in large passenger airliners such as the Airbus 380, Airbus 350XWB and the Boeing 787 [1]. The Airbus A380 still makes use of aluminum alloys as seen in Figure-1 [2] and Boeing's 787 Dreamliner, which is often described as a composite aircraft, contains 20% aluminum alloys (by weight) as shown in Figure-2 [3].



Figure-1. Metal/ fiber applications in the Airbus A380 airplane.

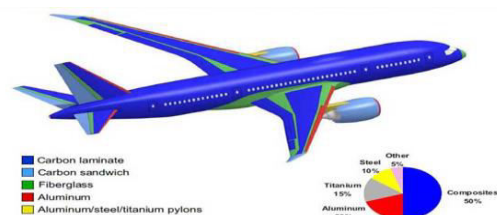


Figure-2. Materials breakdown of the Boeing 787.

The advanced Eurofighter Typhoon also makes use of both aluminum alloys and composites as shown in Figure-3 [4].

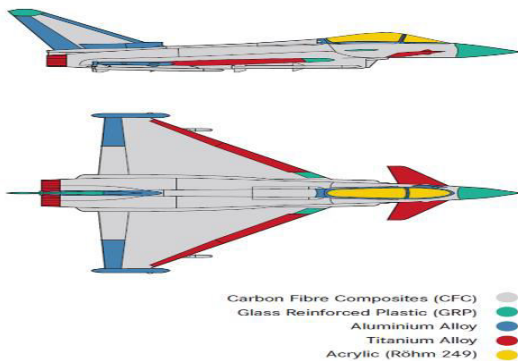


Figure-3. Materials used in the Eurofighter Typhoon airframe.

The aforementioned modern aircrafts use of both composites and aluminum alloys make it imperative to conduct further studies into issues concerning their assemblies hence the relevance of this paper in contributing to such knowledge database.

Furthermore, assembly-induced delaminations were found in the AV-8B and F/A-18 aircrafts where gaps existed between the surface skin, substructures and where the two (surface skin and substructures) were attached with fasteners. Gap conditions in these aircrafts were improved with the proper use of a liquid shim material and with changes in tool geometry, and detail part geometry [5]. The practice in the aerospace industry is to use a liquid shim to fill gaps between 0.13 mm and 0.76 mm, and to use a combination of solid and liquid shim for gaps beyond 0.76 mm [6].

Though there has been some published literature on shimming [7-9], they are skewed toward liquid shims [10-13] and only a few [14] involving both liquid shim and solid shim but carried out experimentally. Even more revealing is that there is not enough published literature on the kind of study conducted in this paper. [15] Conducted a similar study which was skewed towards liquid shim and was for only composite substrates.

The shim materials used in this study are the commercially available liquid-shim materials—Hysol EA9394 [16] and solid peelable fiberglass shims. Liquid shim materials are typically thixotropic epoxy based thermosetting compounds exhibiting: (i) good compression properties, and (ii) resistance to mechanical fatigue. Other important properties of liquid shim materials include viscosity, handling time, drilling-time and fastener-installation-time [12]. Laminated (solid peelable fiberglass) shims—E glass fiber is shims that have peelable layers that allow an engineer to adjust the thickness of the shims right at the assembly line. This means that instead of keeping large stocks of different sized shims or stacking loose shims, an assembly line engineer can peel back the layers of the shim to adjust for tolerances right on the site. In this way, the close tolerances of a precision shim are obtained without the considerable time and expense of precision manufacturing for each shim. AA 7075-T651 was chosen for this study because of its use in the aerospace industry for highly stressed and critical structural parts [17,18]. The other

components were also chosen based on their applications in the aerospace industry.

MATERIALS FOR EXPERIMENTAL TESTING AND MODELING OF THE COMPOSITE-ALUMINUM BOLTED JOINT

The test specimen, as well as the finite element model, were composed of the following parts (Figure-4); a hi-shear corporation fastener with a protruding head (HST-12-8) with a washer all composed of aerospace grade titanium alloy (Ti-6Al-4V-STA), one plate made of CFRP material carbon-epoxy IMS-977-2 (Cytac Industries Inc.) with its quasi-isotropic stacking sequence being $[+45/90/-45/0/90/0/-45/90/+45/-45]_S$ and with a ply thickness of 0.188 mm for 20 plies (total plate thickness being 3.76mm), and the other plate was made of a high strength aerospace grade aluminum alloy, AA 7075 T651. Commercially available liquid-shim material—Hysol EA9394 of Henkel Corporation and a solid peelable fiberglass of LAMECO group manufactured under the Commercial Aircraft Corporation of China (COMAC) standard CMS-MT-301 were incorporated into the assembled model as seen in Figure-5. The simulated model and the test specimen conformed to the composite bearing response and the open-hole tensile strength test standards of American Society for Testing and Materials, D5961/D5961M-13[19] and D5766/D5766M-07 [20] respectively. The open-hole compressive model's geometry of the composite-aluminum bolted joint specimen without any shim material is shown in Figure-4 and that of, with a shim material is shown in Figure-5.

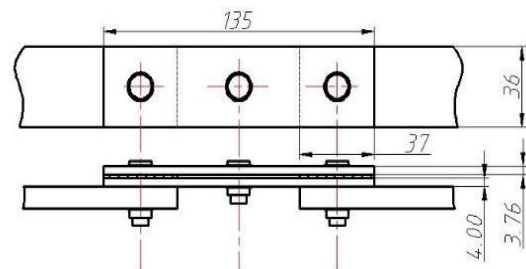


Figure-4. Dimensions in mm for the open-hole composite-aluminum bolted joint compressive model without any shim material.

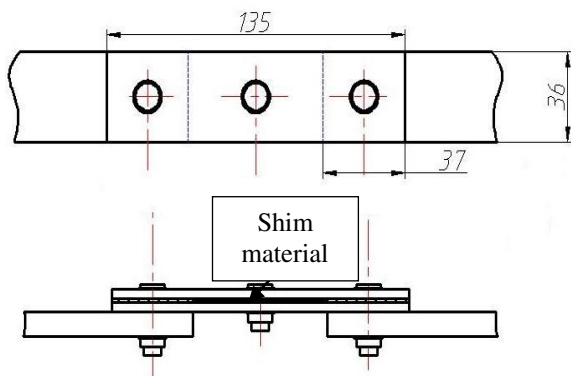


Figure-5. Dimensions in mm for the open-hole composite-aluminum bolted joint compressive model with a shim material.

The open-hole composite-aluminum assembly compressive model was based on a typical assembly error [15] as shown in Figure-6.

The FE model and the test specimen were an idealization of an aircraft's wingbox sub-structural components which are a composite wing panel and an aluminum wing spar.

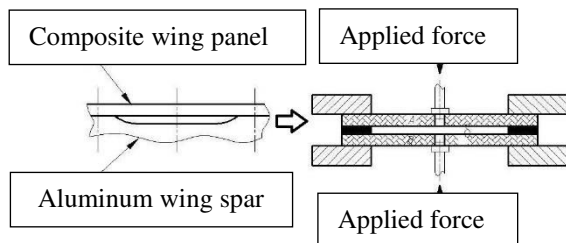
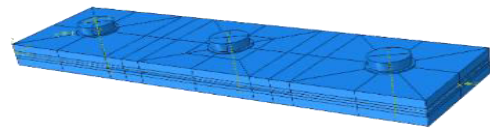


Figure-6. A typical aircraft's wingbox substructure assembly error's geometry.

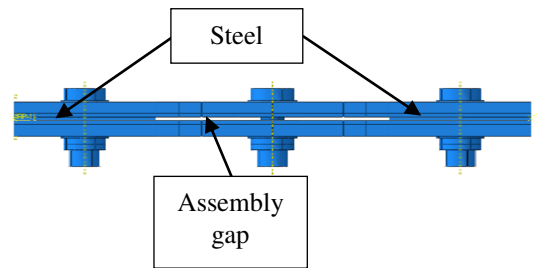
Finite Element model

A non-linear 3-D solid elements model of an open-hole composite-composite and composite-aluminum assembled structures with and without shim layers under static compressive loading were developed using the commercial finite element program ABAQUS/standard 6.13 [21] according to [19,20] configurations. The developed model for a composite-aluminum assembled structure without and with a shim material is shown in Figure-7(a) and Figure-7(b), respectively. The bolt, collar, and the washer were modeled as a unit as shown in Figure-8 because they were engaged together and they are composed of the same titanium material. There were fifteen (15) models in totality each for the composite-composite and composite-aluminum bolted joints. These models are: without shim (0.1mm, 0.3mm, 0.5mm, 0.7mm and 0.9mm thickness), with liquid shim (0.1mm, 0.3mm, 0.5mm, 0.7mm and 0.9mm thickness) and with solid peelable fiberglass (0.1mm, 0.3mm, 0.5mm, 0.7mm and 0.9mm thickness). The plates were cut

($\frac{1}{4}$ of the plate thickness in the z – direction) to avoid overconstraining the assembled structure.



(i) Isometric view



(ii) Side view

Figure-7(a). FE model of composite-aluminum bolted joint compressive model without a shim.

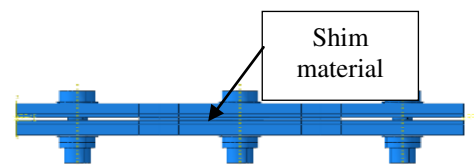


Figure-7(b). FE model of composite-aluminum bolted joint compressive model with a shim.

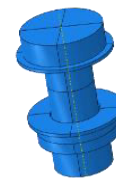


Figure-8. FE model of bolt-collar-washer.

Subsequently presented is a detailed literature on the FE modeling and material properties of specimen used in the modeling.

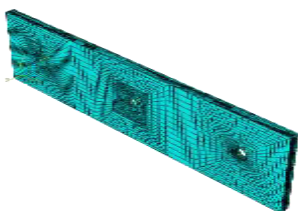
Carbon Fiber-Reinforced Polymer (CFRP) substrate

The strength and elastic properties [22] for the carbon-epoxy IMS-977-2 substrate are shown in Table-1.

**Table-1.** CFRP elastic and strength properties.

Property			
Longitudinal modulus	E_{11}	(GPa)	156
Transverse modulus	E_{22}	(GPa)	8.35
Out-of-plane modulus	E_{33}	(GPa)	8.35
In-plane shear modulus	G_{12}	(GPa)	4.2
Out-of-plane shear modulus	G_{13}	(GPa)	4.2
Out-of-plane shear modulus	G_{23}	(GPa)	2.52
In-plane Poisson's ratio	ν_{12}		0.33
Out-of-plane Poisson's ratio	ν_{13}		0.33
Out-of-plane Poisson's ratio	ν_{23}		0.55
Longitudinal tensile strength	X_T	(MPa)	2500
Longitudinal compressive strength	X_C	(MPa)	1400
Transverse tensile strength	Y_T	(MPa)	75
Transverse compressive strength	Y_C	(MPa)	250
Out-of-plane tensile strength	Z_T	(MPa)	75
Out-of-plane compressive strength	Z_C	(MPa)	250
In-plane shear strength	s_{12}	(MPa)	95
Out-of-plane shear strength	s_{13}	(MPa)	95
Out-of-plane shear strength	s_{23}	(MPa)	108

The CFRP was appropriately partitioned, assigned its material properties after it had been imported into the Abaqus CAE and was modeled with a linear elastic law as an orthotropic material with the orientation for each ply defined. The meshed CFRP plate had a total number of 58400 elements after it has been seeded with 20 elements in the thickness direction (15 elements equally distributed in the area covered by the fastener head, 20 elements equally distributed on the half periphery of the area around the edges of the hole and along the circumferential direction). An approximate global size of 1.5 was used and the box for curvature control checked. A structured hexagonal mesh controls and a stack direction was assigned in the isometric view. The meshed CFRP plate shown as in Figure-9 was modeled using the element type C3D8R: an eight-node linear brick, reduced integration, hourglass control in Abaqus.

**Figure-9.** CFRP meshed finite element model.

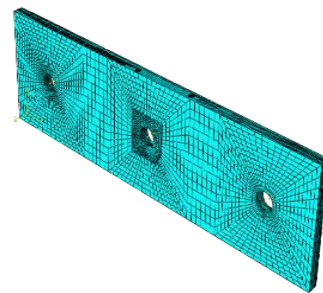
Aluminum alloy, 7075-T651, and Ti-6Al-4V -STA

The aluminum plate and titanium parts were modeled using their elastoplastic material behaviors as shown in Table-2.

Table-2. Elasto-plastic properties of AA7075-T651 [23] and Ti-6Al-4V STA [24].

Elastic properties	AA7075-T651		Ti-6Al-4V STA	
Young's modulus, E (MPa)	71700		110000	
Poisson's ratio, ν	0.306		0.29	
Plastic properties				
Yield stress, σ_y (MPa) and Plastic strain, ϵ_p	σ_y	ϵ_p	σ_y	ϵ_p
	490	0	950	0
	501	0.002	1034	0.002
	561	0.09	1103	0.1

The AA7075-T651 was modeled same as the CFRP plate with the only differences being the seeding in the thickness direction where 10 elements were used and there was no assigning of stacking direction. The meshed AA7075-T651 plate as shown in Figure-10 has a total number of 29080 elements. Titanium parts were also modeled same as the CFRP plate but also with different approximate global size (1.0 used) and mesh controls (sweep used).

**Figure-10.** AA7075-T651 meshed FE model.

The meshed Ti-6Al-4V STA as shown in Figure-11 has 7402 number of elements.

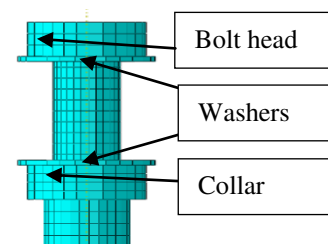
**Figure-11.** Bolt-collar-washer meshed FE model.

Table-3 shows the elastic properties used to model the steel shim and the steel shim has the function of



being used to keep the assembly gap hence it was constraint as a rigid body.

Table-3. Elastic properties of steel shim [25].

Property	
Young's modulus, E (GPa)	210
Poisson's ratio, ν	0.30

The meshed steel shim (0.3mm thickness) as shown in Figure-12 was also modeled same as the CFRP plate but with different approximate global size (2.0 used) and has 351 number of elements.

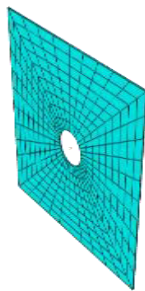


Figure-12. Meshed FE model of 0.3 thickness steel.

Shim material

The Hysol EA9394 of Henkel Corporation and the solid peelable fiberglass were modeled using their elastic properties as shown in Table-4.

Table-4. Elastic properties of Hysol EA9394 [26] and solid peelable fiberglass [27].

Property	Hysol EA9394	solid peelable fiberglass
Young's modulus, E (MPa)	4330	84700
Poisson's ratio, ν	0.35	0.24

The shim materials were modeled same as the CFRP plate but with an approximate global size of 0.7 and seeded with 1 element in the thickness direction for a shim thickness of 0.1mm (3 elements for a shim thickness of 0.3mm, 5 elements for a shim thickness of 0.5mm, 7 elements for a shim thickness of 0.7mm and 9 elements for a shim thickness of 0.9mm). Shown in Figure-13 is a meshed model of a shim with the thickness of 0.3mm and has 10359 number of elements.

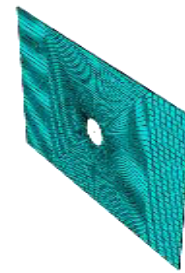


Figure-13. Shim material meshed FE model.

Boundary conditions and contact relationships

The boundary conditions of the FE model as shown in Figure-14 has the surfaces with the 'Reference Node 1' (RP-1) and the 'Reference Node 2' (RP-2) held fixed in all 6 degrees of freedoms (U_x , U_y , U_z , R_x , R_y and R_z).

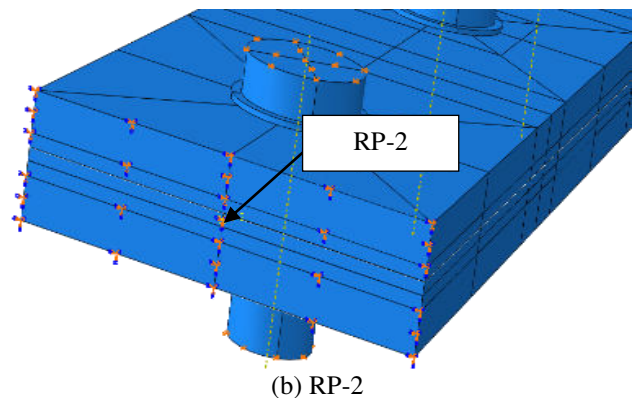
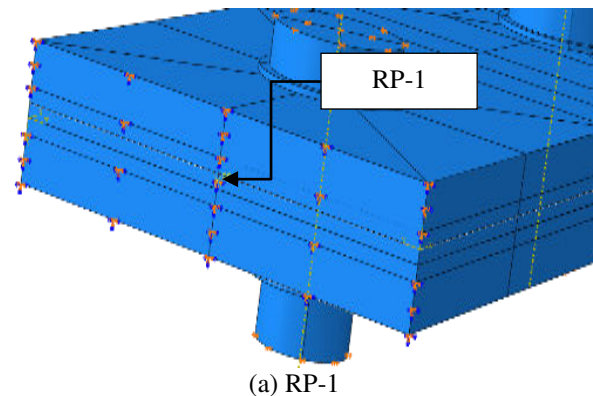
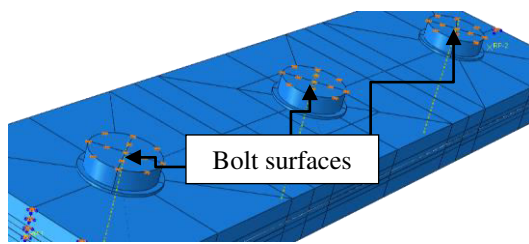
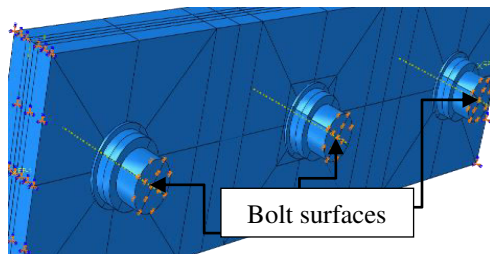


Figure-14. Boundary conditions on the plates.

The upper surfaces of the bolt head and the bottom surfaces were all held fixed in two translational directions (U_x and U_y) as shown in Figure-15.



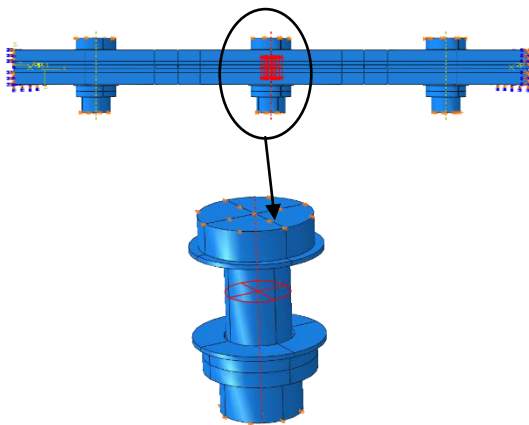
(a) Upper surfaces of bolts



(b) Bottom surfaces of bolts

Figure-15. Boundary conditions on the bolts.

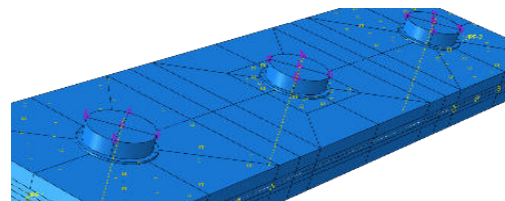
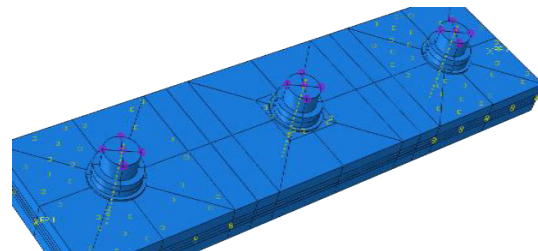
The clamping force of 10KN [28] produced by the tightening torque was applied through a bolt load function in ABAQUS/standard in the U_z direction as shown in Figure-16.

**Figure-16.** Bolt load application.

The contact relationships were defined for contact pairs interacting with each other using a stringent master-to-slave rule [21]. A total of twenty (20) contact pairs were defined and implemented in the FE model under the interaction section in Abaqus. Contact is modelled between (i) the main plates, (ii) between fastener (shanks) and plate holes, (iii) between shim materials and main plates, (iv) between shim materials and fastener shanks, (v) between main plates and washers (upper and bottom surfaces) and (vi) between main plates and steel shim. The contacts were defined using the penalty method with hard contact, frictional coefficients, and finite sliding. "Finite-Sliding" allows for any arbitrary motions of the faying surfaces. The active contact constraints any changes during the analysis. "Small-Sliding" is used if there is a

relatively little sliding of any surfaces interacting with the other.

A surface-to-surface contact option is used for all contacts. Several coefficients of friction were used in the model and their value depends on the components in contact. The frictional coefficient for the interaction between the composite plate and the titanium parts is 0.16 [28]. Frictional coefficients of 0.288 [29] and 0.235 [30] were used for interactions between aluminum plate and titanium parts, and composite plate and aluminum plate respectively. Another frictional coefficient of 0.2 (assumed) was assigned to all parts interacting with the shim materials and a frictional coefficient of 0.16 was also assigned to all other interactions. The surface of the modeled shim was tied onto the composite plate and as shown in Figure-17(a) and Figure-17(b), special elements (springs/dashpots) were used to connect points to ground.

**Figure-17(a).** Springs/dashpots on upper surfaces of bolts.**Figure-17(b).** Springs/dashpots on bottom surfaces of bolts.

EXPERIMENTAL WORK

The experiment was performed under quasi-static compressive loading using an in-house testing equipment which was designed and manufactured in accordance with China National Standards.

Test specimen preparation

The specimens were prepared in accordance with the configurations in [19] and [20]. The liquid shim was prepared in accordance with the manufacturer's instructions and applied to both the aluminum plate and the composite plate. The prepared specimens were clamped and allowed at least four days to cure at room temperature. For the specimens with shim materials, the shim adhered to their mating surfaces (i.e. both the aluminum plate and the composite plate). Shown in Figures-(18) and (19) is an aluminum plate specimen with a liquid shim and a solid shim respectively. The specimen without any shim is shown in Figure-20.



Figure-18. Aluminum plate specimen with a liquid shim.



Figure-19. Aluminum plate specimen with a solid shim.



Figure-20. Aluminum plate specimen without any shim material.

Test set-up and procedure

The test specimens were placed into an in-house test equipment which had force sensors incorporated into it as shown in Figure-21. The test equipment was connected to a force meter (shown in Figure-22) and a little force was applied until zero readings were shown on all the force meters then a final force of 10KN was applied. All tests were performed at room temperature.

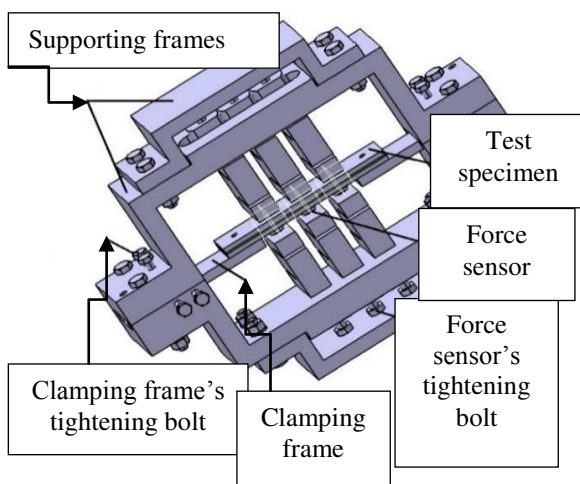


Figure-21. An in-house test equipment.



Figure-22. Force meter.

To be able to compare analytical and experimental results, the specimens were equipped with 6 strain gages as shown in Figures (23) and (24) which temperature self-compensating gages were provided by Huangyan Testing Instrument Factory with its specifications shown in Table-5.

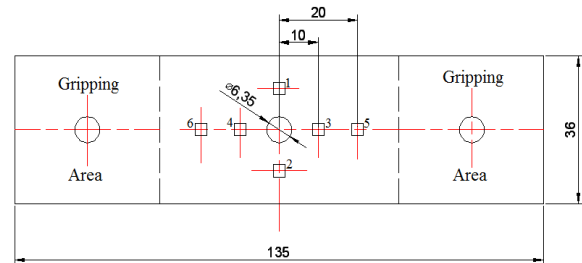


Figure-23. Open hole specimen geometry (all dimensions in mm) and strain gages locations.

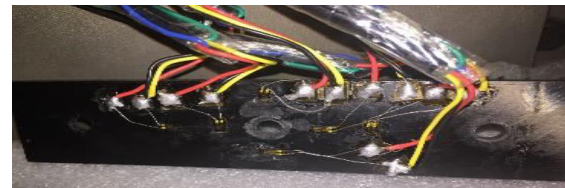


Figure-24. Bonded strain gages on the composite plate.

Each strain gage was connected by a cable to DH3816N (shown in Figure-25) and labeled as a channel.

Table-5. Specifications of strain gages.

Code	Electric resistance/ Ω	Sensitivity coefficient	Gate-length \times gate-width/mm
BHF350-3AA	350 ± 0.30	2.10 ± 1	3×3
Code	Base-length \times base-width/mm	Heat output/ $mm/^\circ C$	Precision grade
BHF350-3AA	7.5×4.5	0.50	A



Figure-25. DH3816N.

The DH3816N was also connected to a computer by means of a local area network (LAN) cable and the computer identified the DH3816N by an internet protocol (IP) address. Figure-26 shows the full set-up of the testing equipment.



Figure-26. Testing equipment set-up.

The test specimens were then rigidly clamped into the testing set-up and an initial load of 0.1KN was applied then with a constant load of 10KN which did not cause any visible damage to the plates. Shown in Figures(27) and (28) is the composite-aluminum test specimen with a liquid shim and a solid shim respectively. And also, the specimen without any shim is shown in Figure-29.

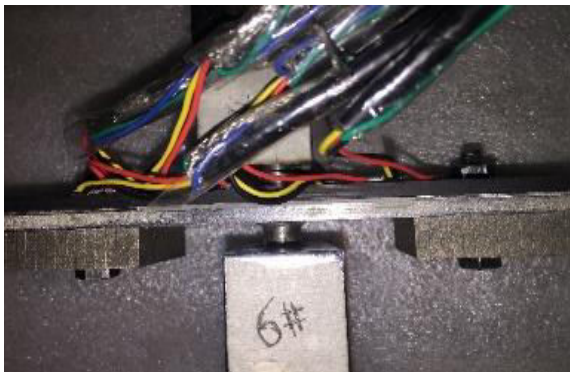


Figure-27. Clamped composite-aluminum test specimen with a liquid shim.



Figure-28. Clamped composite-aluminum test specimen with a solid shim.



Figure-29. Clamped composite-aluminum test specimen without any shim material.

Longitudinal (E_{11}) and transverse (E_{22}) strains were recorded by the computer in micro-strains ($\mu\epsilon$) after three consecutive tests but the results from the FE simulations are in strains (ϵ).

RESULTS AND DISCUSSION

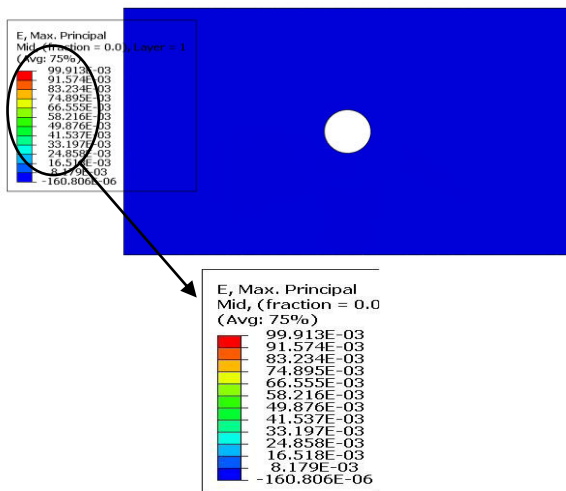
This section presents the contour plots of the Von Mises stresses (S, Mises) and the maximum principal strains (E, Max) of the open-hole compressive FE model. Experimentally determined results for the strains are presented as well.

The effect of strains

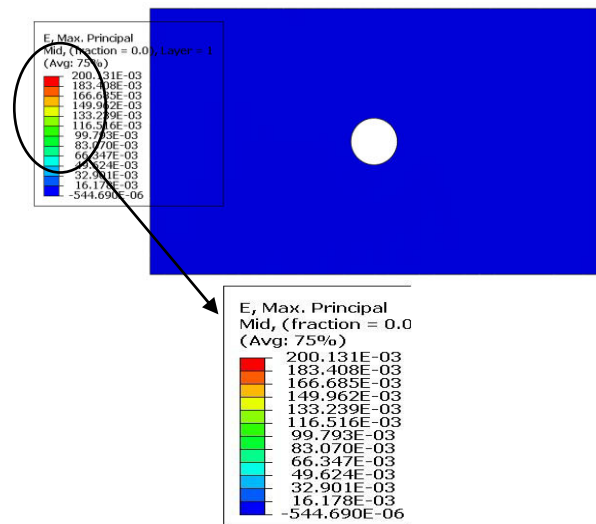
The agreement between the measured strains and the numerically simulated strains is relatively good. It should be noted that the measured strains by the gages located closest to the hole are higher which is explained by the fact that there are higher strain gradients in those areas meaning that the location of the gages is very important.

Composite-composite assembled structure

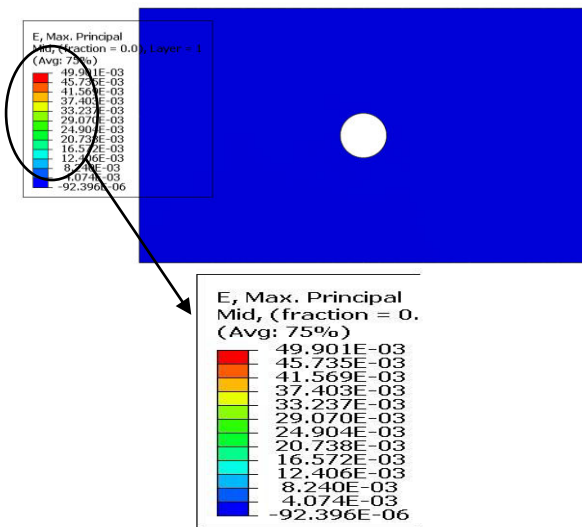
The contour plots of the maximum principal strains (E, Max) as shown in Figures-(30), (31), (32), (33) and (34) is the upper surface (surface interacting with the shim materials) of the bottom plate (composite) for the various assembly gaps (0.1, 0.3, 0.5, 0.7 and 0.9) (all dimensions in mm).



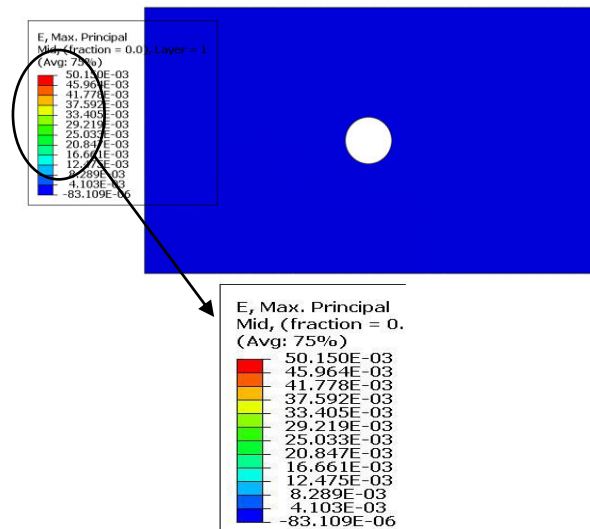
(a) Without any shim material



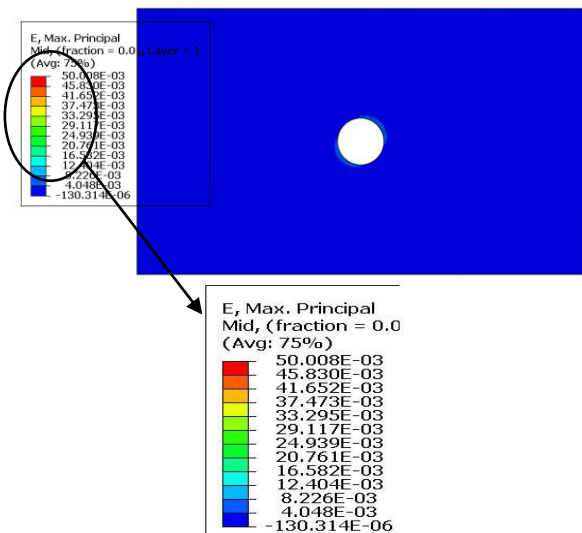
(a) Without any shim material



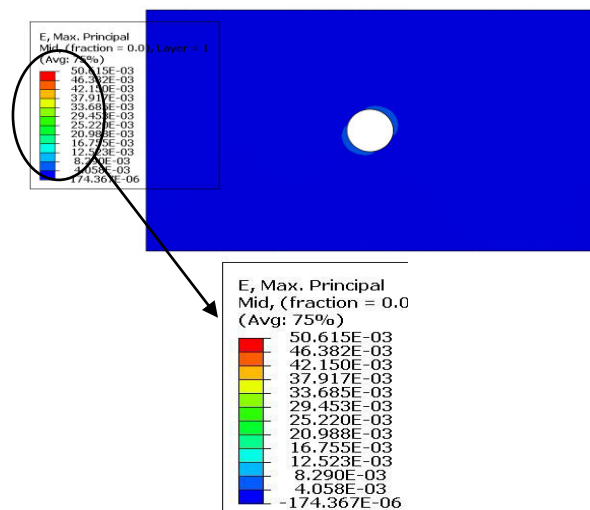
(b) With a liquid shim



(b) With a liquid shim



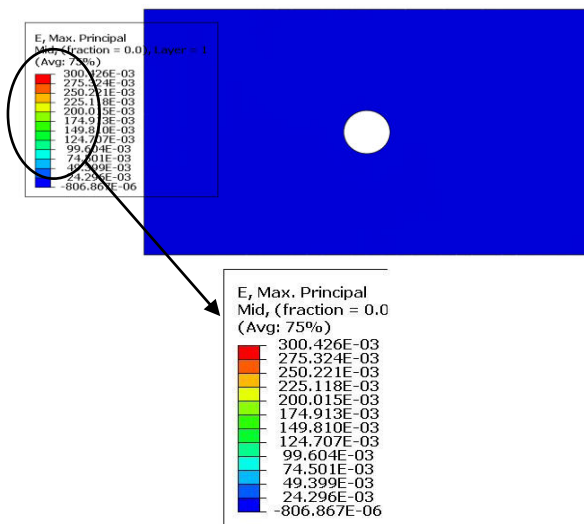
(c) With a solid shim



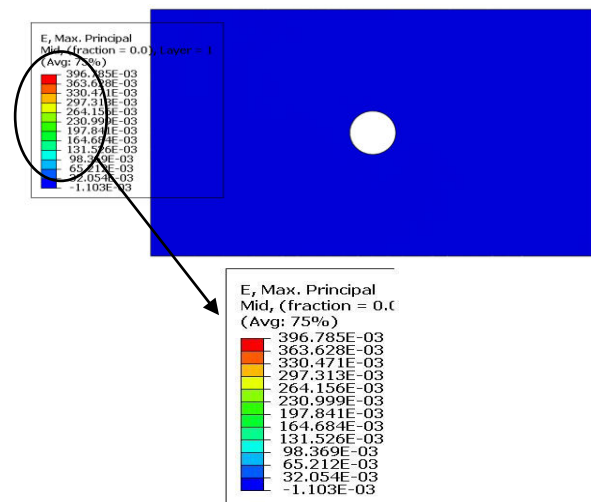
(c) With a solid shim

Figure-30. Strain distribution for an assembly gap of 0.1mm.

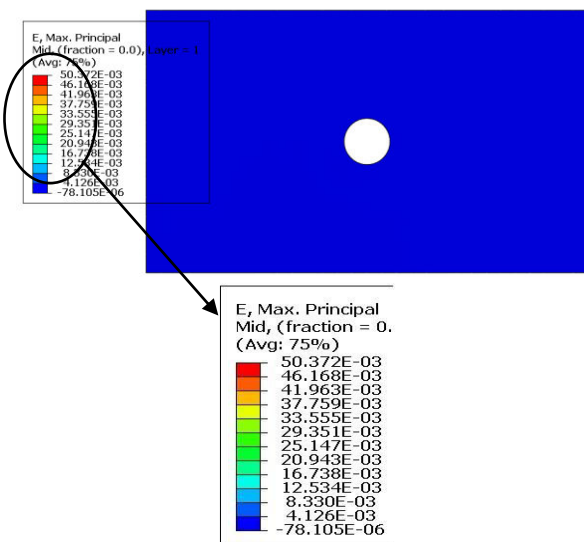
Figure-31. Strain distribution for an assembly gap of 0.3mm.



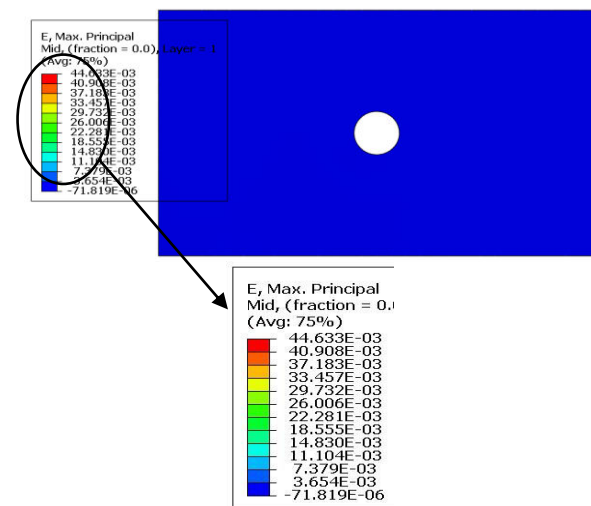
(a) Without any shim material



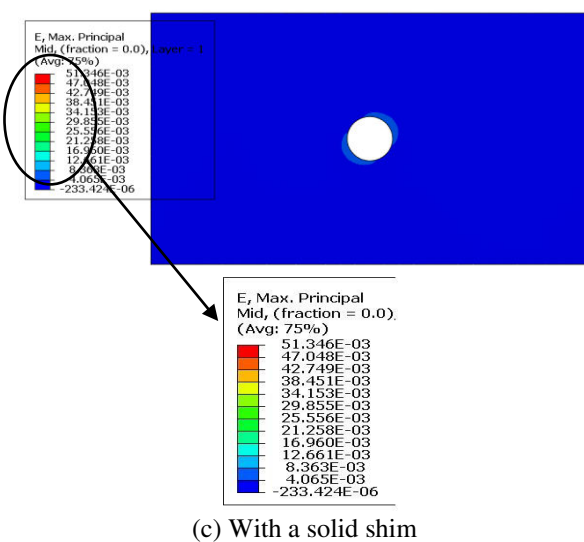
(a) Without any shim material



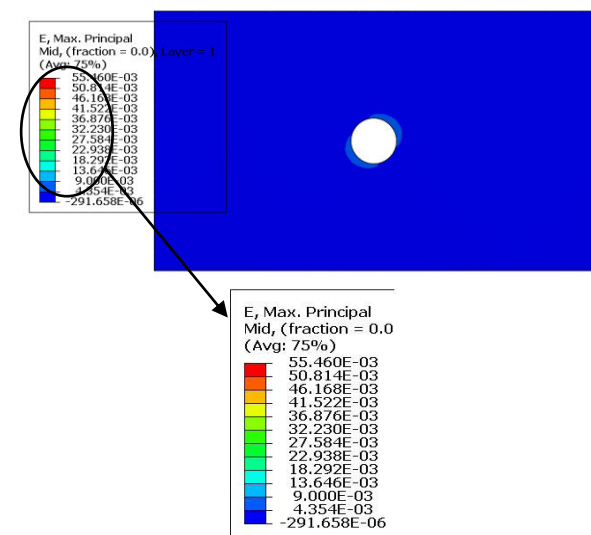
(b) With a liquid shim



(b) With a liquid shim



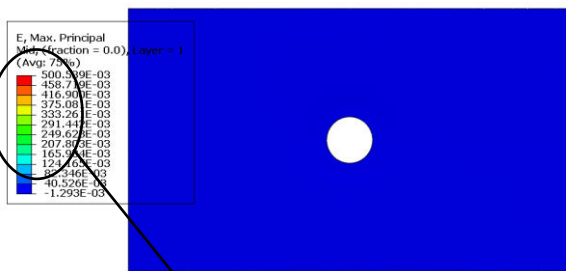
(c) With a solid shim



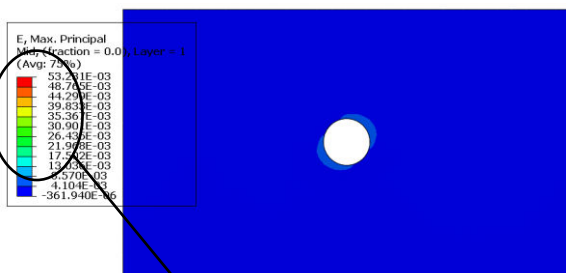
(c) With a solid shim

Figure-32. Strain distribution for an assembly gap of 0.5mm.

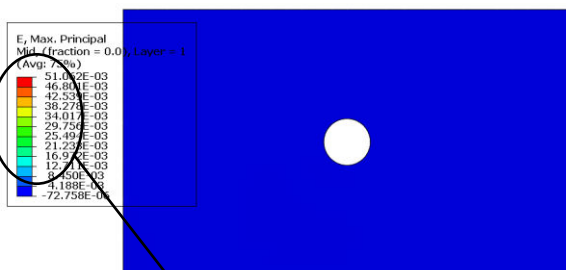
Figure-33. Strain distribution for an assembly gap of 0.7mm.



(a) Without any shim material



(b) With a liquid shim



(c) With a solid shim

Shown in Tables (6), (7) and (8) are the comparisons of the numerical results with the experimental data for assembly gaps without any shim materials, liquid shim, and solid peelable fiberglass shim respectively.

Table-6. Comparison of the various strains with experimental data for the assembly gaps without any shim materials.

(a) Data

Gap thickness	Gages	Average experimental values ($\mu\epsilon$)	Numerically simulated values ($\mu\epsilon$)
0.1	1(E_{11})	-123.98	-129.98
	2(E_{22})	146.00	156.00
	3(E_{22})	376.14	386.09
	4(E_{11})	-507.74	-548.86
	5(E_{11})	-384.85	-412.81
	6(E_{22})	167.03	183.04
0.3	1(E_{11})	-126.98	-130.96
	2(E_{22})	218.05	238.07
	3(E_{22})	370.14	401.20
	4(E_{11})	-470.78	-488.76
	5(E_{11})	-923.18	-1004.91
	6(E_{22})	188.04	197.19
0.5	1(E_{11})	-184.97	-195.96
	2(E_{22})	320.10	347.20
	3(E_{22})	477.23	498.16
	4(E_{11})	-623.61	-642.60
	5(E_{11})	-1029.94	-1081.83
	6(E_{22})	286.08	298.09
0.7	1(E_{11})	-161.97	-172.96
	2(E_{22})	674.54	687.85
	3(E_{22})	667.44	684.47
	4(E_{11})	-675.54	-690.52
	5(E_{11})	-1981.07	-2034.85
	6(E_{22})	466.22	504.02
0.9	1(E_{11})	-159.97	-169.98
	2(E_{22})	415.33	448.26
	3(E_{22})	778.61	823.68
	4(E_{11})	-853.27	-861.26
	5(E_{11})	-2504.71	-2603.21
	6(E_{22})	530.28	579.34

Figure-34. Strain distribution for an assembly gap of 0.9mm.



(b) Error percentage

Gap thickness	Gages	Error (%)
0.1	1(E_{11})	4.8
	2(E_{22})	6.8
	3(E_{22})	2.6
	4(E_{11})	8.1
	5(E_{11})	7.3
	6(E_{22})	9.6
0.3	1(E_{11})	7.9
	2(E_{22})	9.2
	3(E_{22})	8.4
	4(E_{11})	3.8
	5(E_{11})	8.9
	6(E_{22})	4.9
0.5	1(E_{11})	5.9
	2(E_{22})	8.5
	3(E_{22})	4.4
	4(E_{11})	3.1
	5(E_{11})	5.0
	6(E_{22})	4.2
0.7	1(E_{11})	6.8
	2(E_{22})	2.0
	3(E_{22})	2.6
	4(E_{11})	2.2
	5(E_{11})	2.7
	6(E_{22})	8.1
0.9	1(E_{11})	6.3
	2(E_{22})	7.9
	3(E_{22})	5.8
	4(E_{11})	0.9
	5(E_{11})	3.9
	6(E_{22})	9.3

Table-7. Comparison of the various strains with experimental data for the assembly gaps with liquid shims.

(a) Data

Gap thickness	Gages	Average experimental values ($\mu\epsilon$)	Numerically simulated values ($\mu\epsilon$)
0.1	1(E_{11})	-101.99	-111.98
	2(E_{22})	103.01	107.06
	3(E_{22})	303.09	320.10
	4(E_{11})	-361.87	-378.86
	5(E_{11})	-155.98	-162.81
	6(E_{22})	120.01	128.02
0.3	1(E_{11})	-87.99	-96.00
	2(E_{22})	123.00	135.00
	3(E_{22})	277.08	301.20
	4(E_{11})	-441.80	-457.79
	5(E_{11})	-844.29	-873.18
	6(E_{22})	-146.98	-157.19
0.5	1(E_{11})	-145.98	-154.96
	2(E_{22})	283.92	290.98
	3(E_{22})	365.13	400.16
	4(E_{11})	-554.69	-573.68
	5(E_{11})	-512.74	-561.83
	6(E_{22})	177.03	184.07
0.7	1(E_{11})	-83.99	-89.97
	2(E_{22})	594.35	644.47
	3(E_{22})	401.16	433.12
	4(E_{11})	-568.68	-594.65
	5(E_{11})	-442.80	-484.91
	6(E_{22})	353.12	387.05
0.9	1(E_{11})	-130.98	-143.98
	2(E_{22})	281.07	301.06
	3(E_{22})	492.22	532.28
	4(E_{11})	-624.61	-653.57
	5(E_{11})	-743.45	-779.39
	6(E_{22})	184.03	205.02



(b) Error percentage

Gap thickness	Gages	Error (%)
0.1	1(E_{11})	9.8
	2(E_{22})	3.9
	3(E_{22})	5.6
	4(E_{11})	4.7
	5(E_{11})	4.4
	6(E_{22})	6.7
0.3	1(E_{11})	9.1
	2(E_{22})	9.8
	3(E_{22})	8.7
	4(E_{11})	3.6
	5(E_{11})	3.4
	6(E_{22})	6.9
0.5	1(E_{11})	6.2
	2(E_{22})	2.5
	3(E_{22})	9.6
	4(E_{11})	3.4
	5(E_{11})	9.6
	6(E_{22})	4.0
0.7	1(E_{11})	7.1
	2(E_{22})	8.4
	3(E_{22})	8.0
	4(E_{11})	4.6
	5(E_{11})	9.5
	6(E_{22})	9.6
0.9	1(E_{11})	9.9
	2(E_{22})	7.1
	3(E_{22})	8.1
	4(E_{11})	4.6
	5(E_{11})	4.8
	6(E_{22})	11.4

Table-8. Comparison of the various strains with experimental data for the assembly gaps with solid shims.

(a) Data

Gap thickness	Gages	Average experimental values ($\mu\epsilon$)	Numerically simulated values ($\mu\epsilon$)
0.1	1(E_{11})	-117.95	-126.92
	2(E_{22})	139.29	144.30
	3(E_{22})	304.90	322.05
	4(E_{11})	-399.64	-438.59
	5(E_{11})	-239.96	-273.99
	6(E_{22})	141.07	166.09
0.3	1(E_{11})	-96.95	-108.91
	2(E_{22})	194.24	225.09
	3(E_{22})	331.28	377.46
	4(E_{11})	-458.02	-473.05
	5(E_{11})	-901.64	-971.62
	6(E_{22})	159.07	176.05
0.5	1(E_{11})	-180.92	-189.90
	2(E_{22})	304.16	337.22
	3(E_{22})	441.55	482.68
	4(E_{11})	-609.00	-636.01
	5(E_{11})	-884.50	-997.85
	6(E_{22})	255.21	283.05
0.7	1(E_{11})	-117.90	-139.91
	2(E_{22})	670.45	677.46
	3(E_{22})	621.39	658.43
	4(E_{11})	-637.12	-673.05
	5(E_{11})	-906.91	-1050.88
	6(E_{22})	428.28	454.21
0.9	1(E_{11})	-112.85	-128.89
	2(E_{22})	244.41	289.66
	3(E_{22})	476.77	499.00
	4(E_{11})	-604.73	-617.75
	5(E_{11})	-569.68	-649.58
	6(E_{22})	127.18	149.42

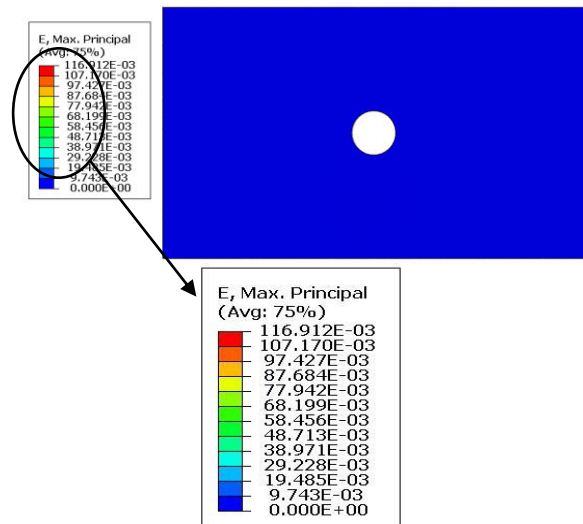


(b) Error percentage

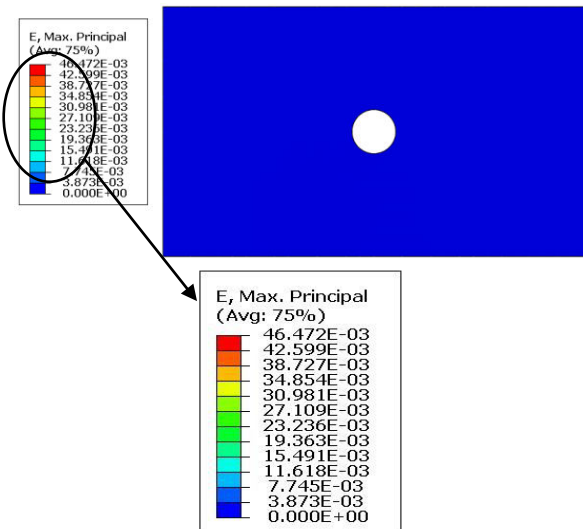
Gap thickness	Gages	Error (%)
0.1	1(E_{11})	7.6
	2(E_{22})	3.6
	3(E_{22})	5.6
	4(E_{11})	8.9
	5(E_{11})	14.2
	6(E_{22})	17.7
0.3	1(E_{11})	12.3
	2(E_{22})	15.9
	3(E_{22})	13.9
	4(E_{11})	3.3
	5(E_{11})	7.8
	6(E_{22})	10.7
0.5	1(E_{11})	5.0
	2(E_{22})	10.9
	3(E_{22})	9.3
	4(E_{11})	4.4
	5(E_{11})	12.8
	6(E_{22})	10.9
0.7	1(E_{11})	18.7
	2(E_{22})	1.1
	3(E_{22})	6.0
	4(E_{11})	5.6
	5(E_{11})	15.9
	6(E_{22})	6.1
0.9	1(E_{11})	14.2
	2(E_{22})	18.5
	3(E_{22})	4.7
	4(E_{11})	2.2
	5(E_{11})	14.0
	6(E_{22})	17.5

Composite-aluminum assembled structure

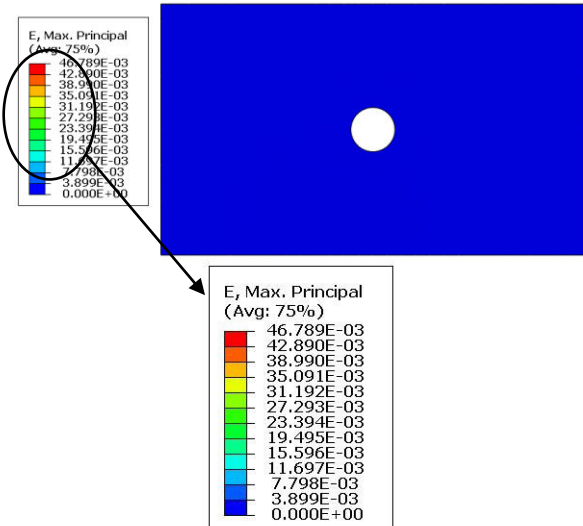
The contour plots of the maximum principal strains (E, Max) as shown in Figures (35), (36), (37), (38) and (39) is the upper surface (surface interacting with the shim materials) of the bottom plate (aluminum) for the various assembly gaps (0.1, 0.3, 0.5, 0.7 and 0.9) (all dimensions in mm).



(a) Without any shim material

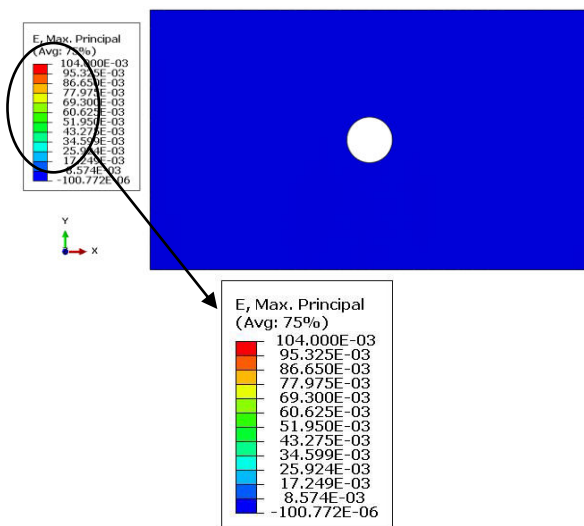


(b) With a liquid shim

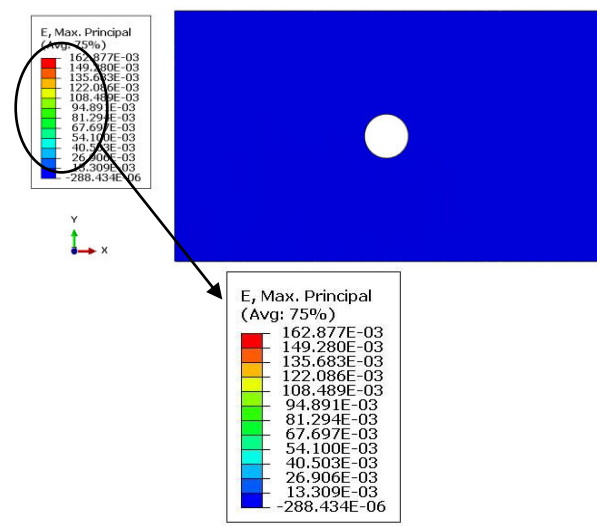


(c) With a solid shim

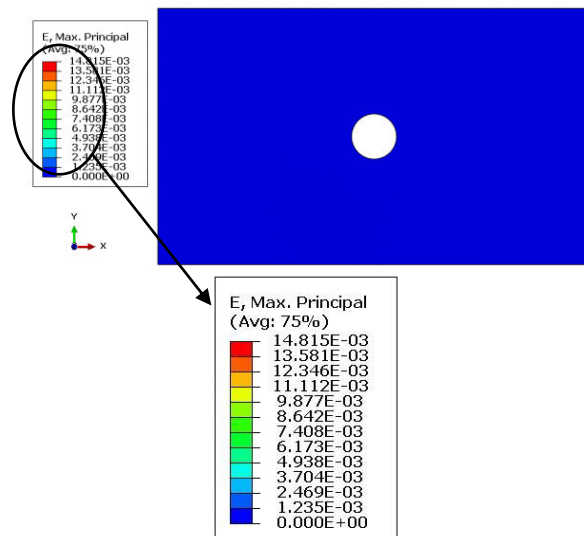
Figure-35. Strain distribution for an assembly gap of 0.1mm.



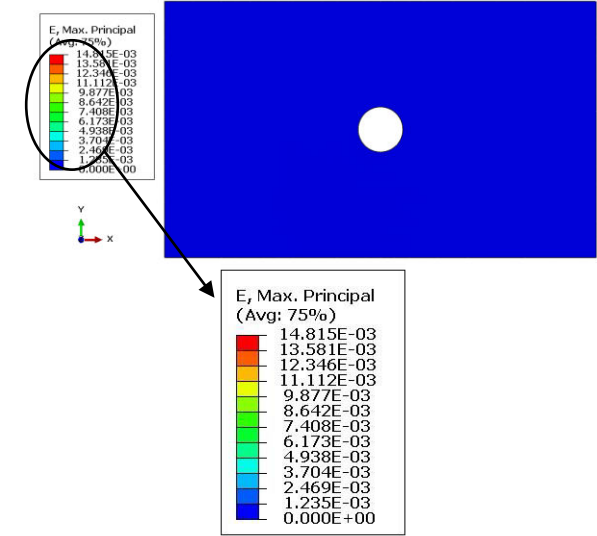
(a) Without any shim material



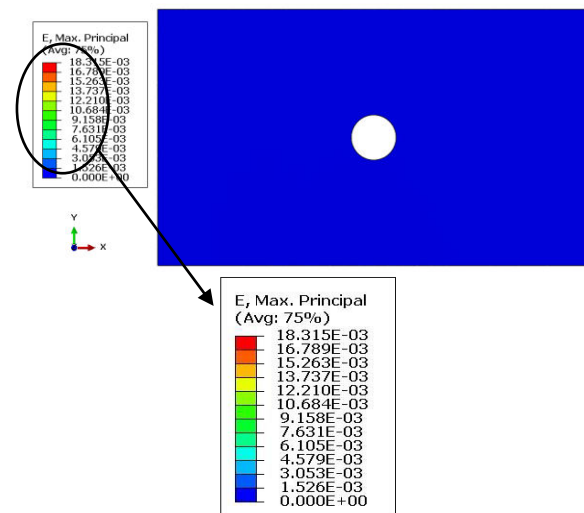
(a) Without any shim material



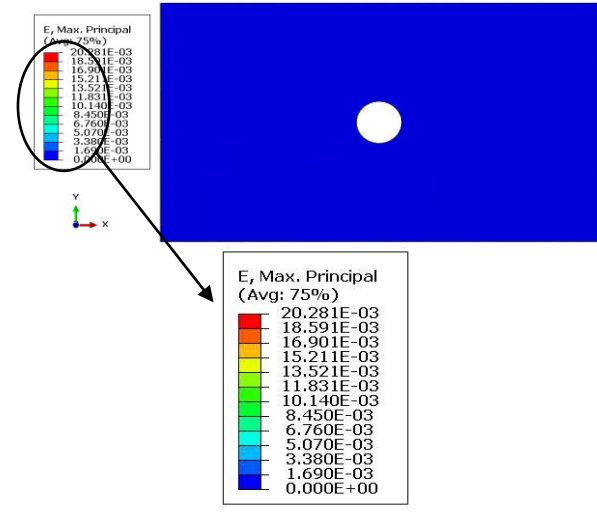
(b) With a liquid shim



(b) With a liquid shim



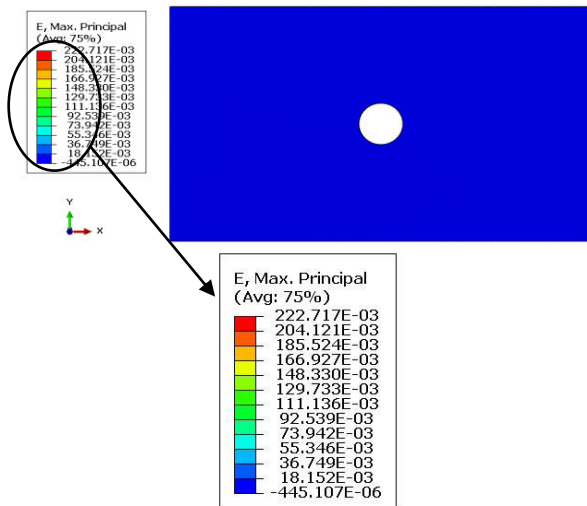
(c) With a solid shim



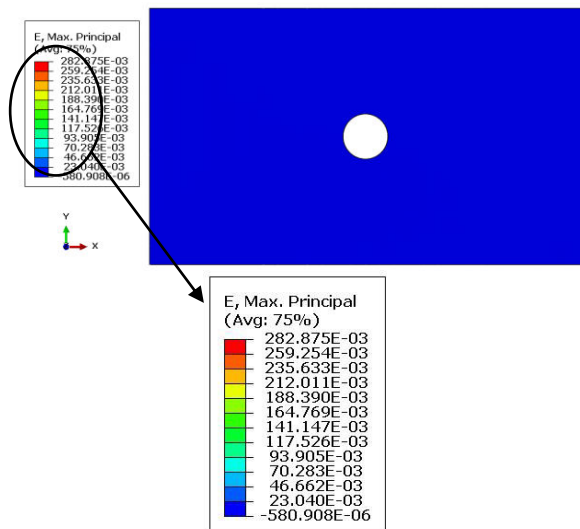
(c) With a solid shim

Figure-36. Strain distribution for an assembly gap of 0.3mm.

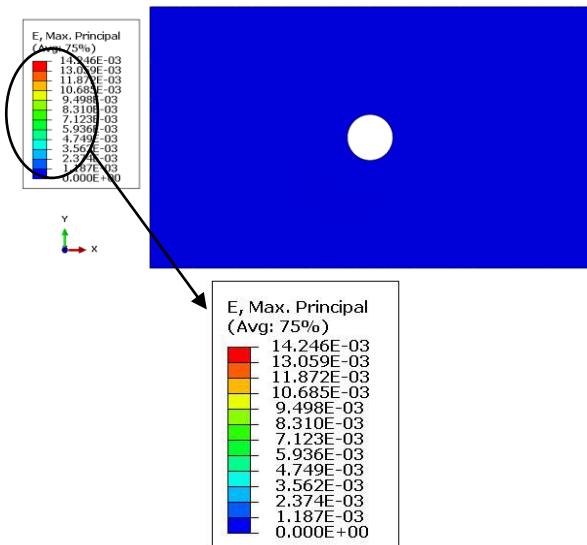
Figure-37. Strain distribution for an assembly gap of 0.5mm.



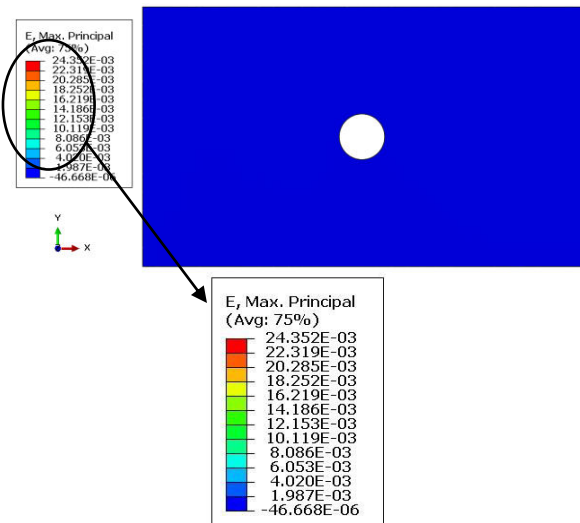
(a) Without any shim material



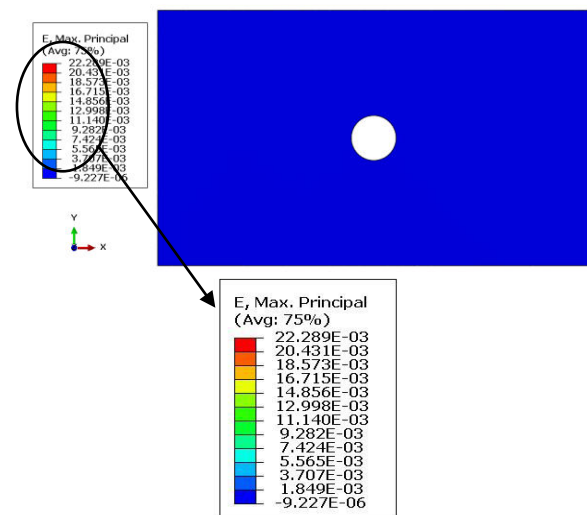
(a) Without any shim material



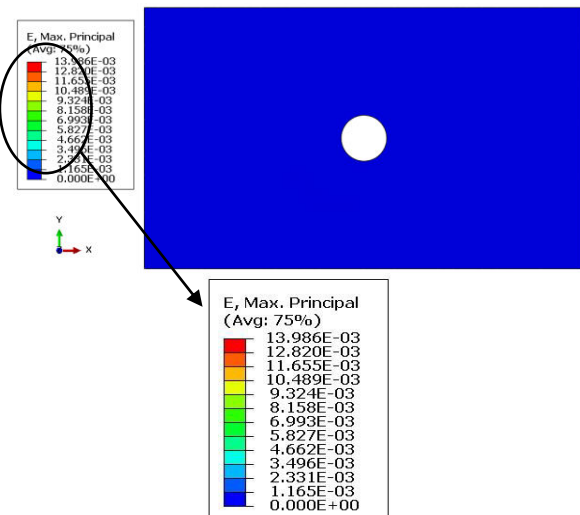
(b) With a liquid shim



(b) With a liquid shim



(c) With a solid shim



(c) With a solid shim

Figure-38. Strain distribution for an assembly gap of 0.7mm.**Figure-39.** Strain distribution for an assembly gap of 0.9mm.



Shown in Tables-(9), (10) and (11) are the comparisons of the numerical results with the experimental data for assembly gaps without any shim materials, liquid shim, and solid peelable fiberglass shim, respectively.

Table-9. Comparison of the various strains with experimental data for the assembly gaps without any shim materials.

(a) Data

Gap thickness	Gages	Average experimental values ($\mu\epsilon$)	Numerically simulated values ($\mu\epsilon$)
0.1	1(E_{11})	-162.97	-175.95
	2(E_{22})	214.05	228.00
	3(E_{22})	390.04	403.70
	4(E_{11})	-577.86	-604.84
	5(E_{11})	-414.90	-446.87
	6(E_{22})	200.28	217.02
0.3	1(E_{11})	-154.98	-169.97
	2(E_{22})	252.95	277.91
	3(E_{22})	394.09	424.11
	4(E_{11})	-562.68	-586.66
	5(E_{11})	-996.22	-1094.37
	6(E_{22})	219.01	236.03
0.5	1(E_{11})	-183.97	-195.98
	2(E_{22})	323.73	349.88
	3(E_{22})	528.18	571.22
	4(E_{11})	-685.53	-708.5
	5(E_{11})	-1380.28	-1493.77
	6(E_{22})	317.26	344.15
0.7	1(E_{11})	-177.99	-193.94
	2(E_{22})	726.32	757.08
	3(E_{22})	675.56	706.5
	4(E_{11})	-691.62	-728.60
	5(E_{11})	-2852.84	-3012.90
	6(E_{22})	491.22	539.13
0.9	1(E_{11})	-187.96	-201.97
	2(E_{22})	1291.33	1416.99
	3(E_{22})	1288.66	1375.89
	4(E_{11})	-1045.90	-1097.86
	5(E_{11})	-4566.06	-4941.46
	6(E_{22})	778.59	851.73

(b) Error percentage

Gap thickness	Gages	Error (%)
0.1	1(E_{11})	8.0
	2(E_{22})	6.5
	3(E_{22})	3.5
	4(E_{11})	4.7
	5(E_{11})	7.7
	6(E_{22})	8.4
0.3	1(E_{11})	9.7
	2(E_{22})	9.9
	3(E_{22})	7.6
	4(E_{11})	4.3
	5(E_{11})	9.9
	6(E_{22})	7.8
0.5	1(E_{11})	6.5
	2(E_{22})	8.1
	3(E_{22})	8.1
	4(E_{11})	3.4
	5(E_{11})	8.2
	6(E_{22})	8.5
0.7	1(E_{11})	9.0
	2(E_{22})	4.2
	3(E_{22})	4.6
	4(E_{11})	5.3
	5(E_{11})	5.6
	6(E_{22})	9.8
0.9	1(E_{11})	7.5
	2(E_{22})	9.7
	3(E_{22})	6.8
	4(E_{11})	5.0
	5(E_{11})	8.2
	6(E_{22})	9.4

**Table-10.** Comparison of the various strains with experimental data for the assembly gaps with liquid shims.

(a) Data

Gap thickness	Gages	Average experimental values ($\mu\epsilon$)	Numerically simulated values ($\mu\epsilon$)
0.1	1(E_{11})	-116.99	-127.94
	2(E_{22})	188.15	199.09
	3(E_{22})	316.11	347.16
	4(E_{11})	-361.87	-378.86
	5(E_{11})	-237.89	-254.68
	6(E_{22})	126.02	133.04
0.3	1(E_{11})	-126.98	-138.97
	2(E_{22})	137.19	150.36
	3(E_{22})	308.60	339.06
	4(E_{11})	-512.74	-537.71
	5(E_{11})	-915.99	-1002.90
	6(E_{22})	185.07	200.02
0.5	1(E_{11})	-159.00	-171.02
	2(E_{22})	294.85	319.36
	3(E_{22})	409.51	421.43
	4(E_{11})	-580.66	-609.75
	5(E_{11})	-742.46	-816.27
	6(E_{22})	189.48	206.59
0.7	1(E_{11})	-95.91	-102.92
	2(E_{22})	603.87	656.84
	3(E_{22})	430.11	447.12
	4(E_{11})	-577.67	-625.61
	5(E_{11})	-629.60	-692.02
	6(E_{22})	385.00	406.35
0.9	1(E_{11})	-155.98	-170.96
	2(E_{22})	654.43	687.47
	3(E_{22})	523.18	559.21
	4(E_{11})	-645.70	-686.68
	5(E_{11})	-751.43	-819.62
	6(E_{22})	248.02	263.06

(b) Error percentage

Gap thickness	Gages	Error (%)
0.1	1(E_{11})	9.4
	2(E_{22})	5.8
	3(E_{22})	9.8
	4(E_{11})	4.7
	5(E_{11})	7.1
	6(E_{22})	5.6
0.3	1(E_{11})	9.4
	2(E_{22})	9.6
	3(E_{22})	9.9
	4(E_{11})	4.9
	5(E_{11})	9.5
	6(E_{22})	8.1
0.5	1(E_{11})	7.6
	2(E_{22})	8.3
	3(E_{22})	2.9
	4(E_{11})	5.0
	5(E_{11})	9.9
	6(E_{22})	9.0
0.7	1(E_{11})	7.3
	2(E_{22})	8.8
	3(E_{22})	4.0
	4(E_{11})	8.3
	5(E_{11})	9.9
	6(E_{22})	5.5
0.9	1(E_{11})	9.6
	2(E_{22})	5.1
	3(E_{22})	6.9
	4(E_{11})	6.3
	5(E_{11})	9.1
	6(E_{22})	6.1

**Table-11.** Comparison of the various strains with experimental data for the assembly gaps with solid shims.

(a) Data

Gap thickness	Gages	Average experimental values ($\mu\epsilon$)	Numerically simulated values ($\mu\epsilon$)
0.1	1(E_{11})	-120.96	-139.20
	2(E_{22})	202.46	216.10
	3(E_{22})	324.87	378.23
	4(E_{11})	-383.27	-450.82
	5(E_{11})	-286.53	-297.59
	6(E_{22})	132.02	151.20
0.3	1(E_{11})	-131.90	-148.82
	2(E_{22})	192.36	216.92
	3(E_{22})	325.13	369.32
	4(E_{11})	-534.92	-546.09
	5(E_{11})	-934.05	-1017.41
	6(E_{22})	192.01	207.41
0.5	1(E_{11})	-161.89	-180.88
	2(E_{22})	303.95	331.06
	3(E_{22})	411.66	451.56
	4(E_{11})	-595.43	-622.47
	5(E_{11})	-789.38	-875.23
	6(E_{22})	209.17	239.11
0.7	1(E_{11})	-103.68	-118.74
	2(E_{22})	655.22	689.44
	3(E_{22})	517.03	533.07
	4(E_{11})	-592.77	-646.84
	5(E_{11})	-704.92	-789.31
	6(E_{22})	398.14	439.05
0.9	1(E_{11})	-112.48	-137.30
	2(E_{22})	565.32	661.92
	3(E_{22})	421.02	445.50
	4(E_{11})	-472.87	-514.96
	5(E_{11})	-610.07	-687.82
	6(E_{22})	187.47	235.19

(b) Error percentage

Gap thickness	Gages	Error (%)
0.1	1(E_{11})	15.1
	2(E_{22})	6.7
	3(E_{22})	16.4
	4(E_{11})	17.6
	5(E_{11})	3.9
	6(E_{22})	14.5
0.3	1(E_{11})	12.8
	2(E_{22})	12.8
	3(E_{22})	13.6
	4(E_{11})	2.1
	5(E_{11})	8.9
	6(E_{22})	8.0
0.5	1(E_{11})	11.7
	2(E_{22})	8.9
	3(E_{22})	9.7
	4(E_{11})	4.5
	5(E_{11})	10.9
	6(E_{22})	14.3
0.7	1(E_{11})	14.5
	2(E_{22})	5.2
	3(E_{22})	3.1
	4(E_{11})	9.1
	5(E_{11})	12.0
	6(E_{22})	10.3
0.9	1(E_{11})	22.1
	2(E_{22})	17.1
	3(E_{22})	5.8
	4(E_{11})	8.9
	5(E_{11})	12.7
	6(E_{22})	25.5

Examining the values in Tables(6), (7), (8), (9), (10) and (11), the following observations were obvious:

- the simulated values corresponded relatively well with the experimental values.
- higher strain values were measured for specimen without any shim materials and the specimen with liquid shim measured relatively lesser values for the assembly gaps 0.1, 0.3, 0.5 and 0.7 (all dimensions in mm). For the 0.9mm assembly gap, the specimen with solid shim material rather measured relatively lesser



values compared with the specimen with liquid shim material.

- c) there were generally increasing measured strain values for an increasing assembly gaps.
- d) interestingly, the error percentages were relatively higher in the comparison of the simulated values with the experimental values for solid shims than that of the liquid shims. This can be as a result of the material properties, mesh densities, boundary conditions, frictional coefficients or experimental errors. Hence care must be taken in modeling and in experimental testing.

The effect of stresses

The results referred in the graphs in this section is the Von Mises stresses (S, Mises) (MPa).

Composite-composite assembled structure

The contour plots of the Von Mises stresses (S, Mises) as shown in Figures (40), (41), (42), (43) and (44) is the upper surface (surface interacting with the shim materials) of the bottom plate (composite) for the various assembly gaps (0.1, 0.3, 0.5, 0.7 and 0.9) (all dimensions in mm).

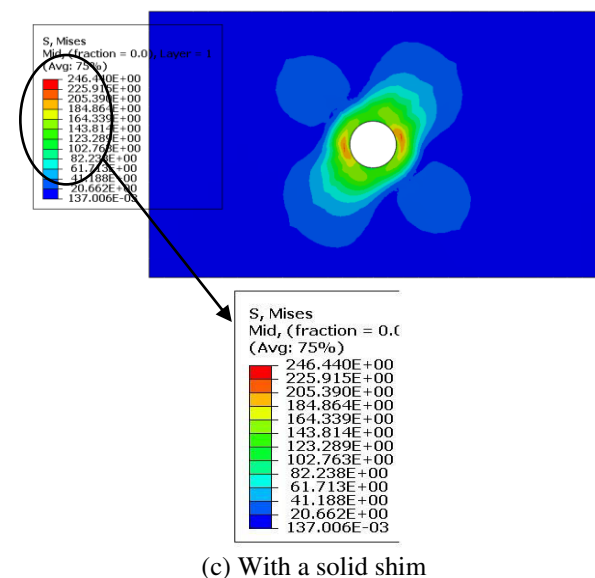
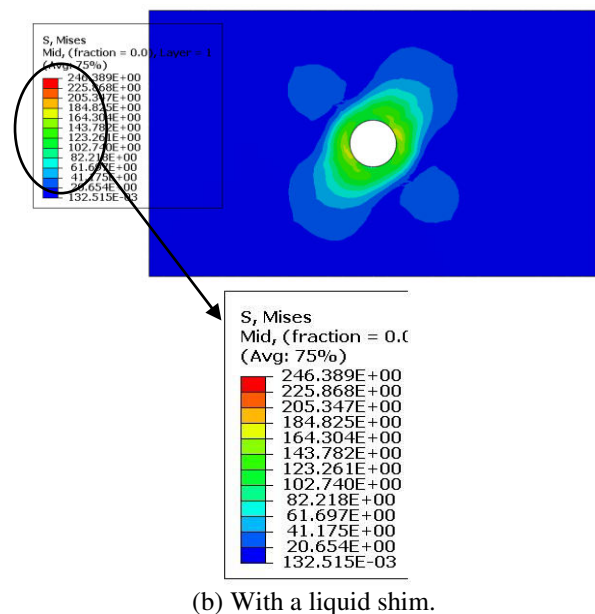
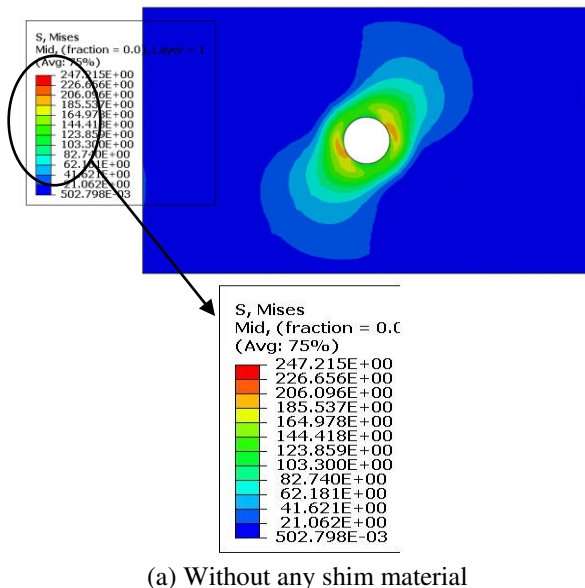
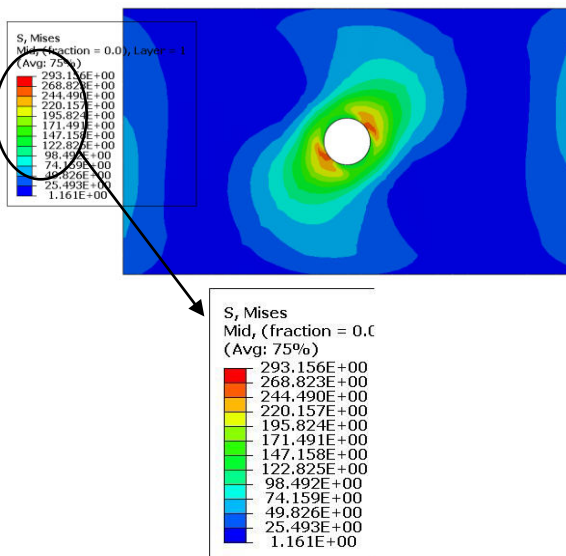
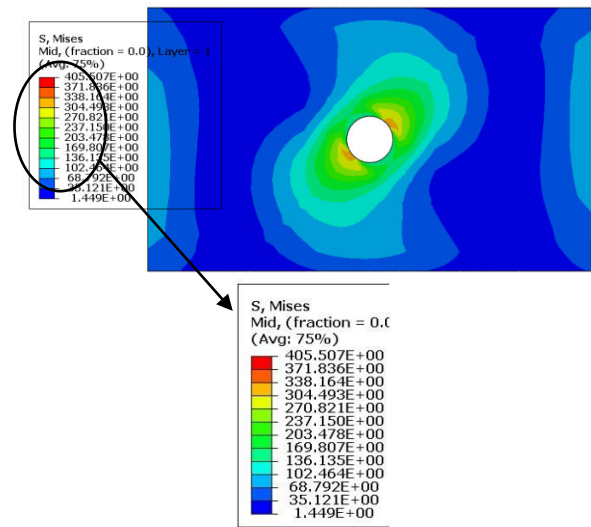


Figure-40. Stress distribution for an assembly gap of 0.1mm.

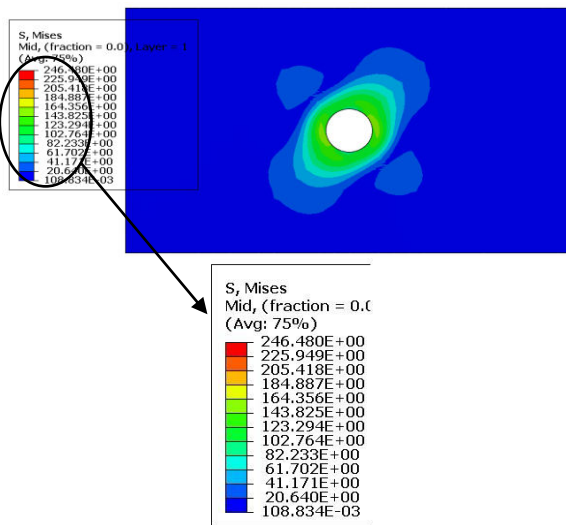




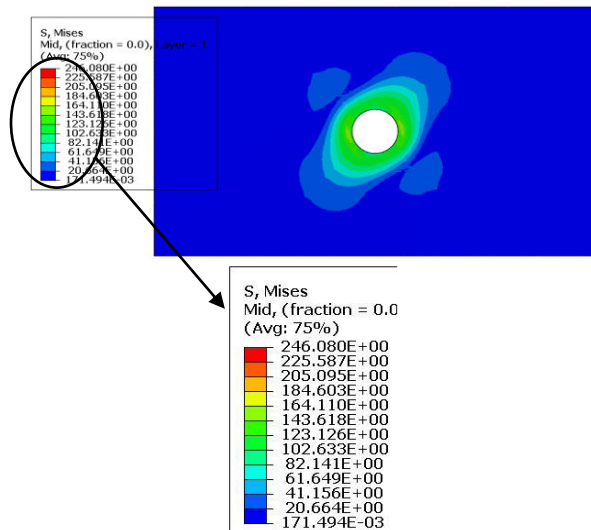
(a) Without any shim material



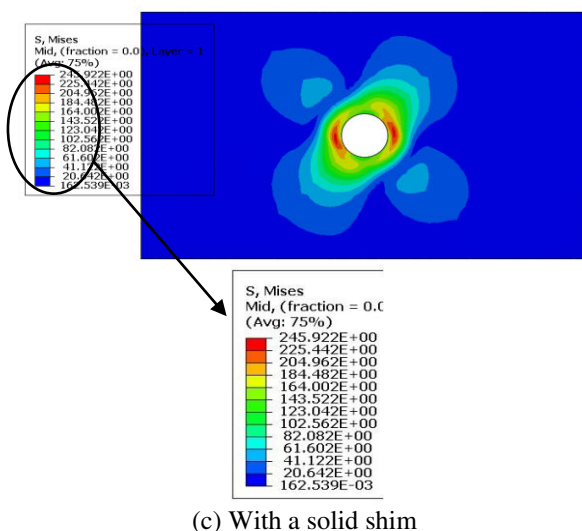
(a) Without any shim material



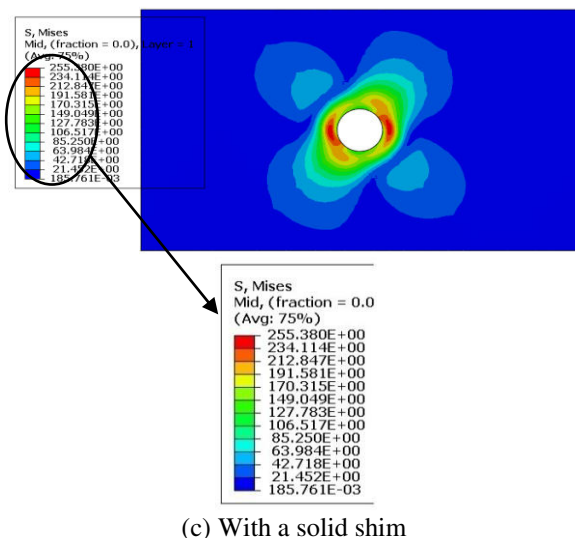
(b) With a liquid shim



(b) With a liquid shim

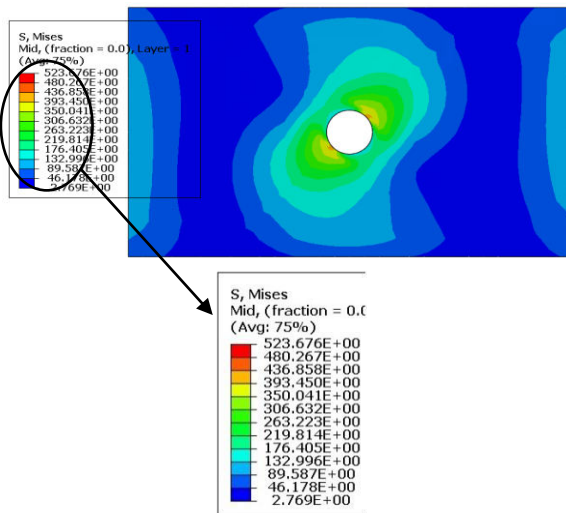


(c) With a solid shim

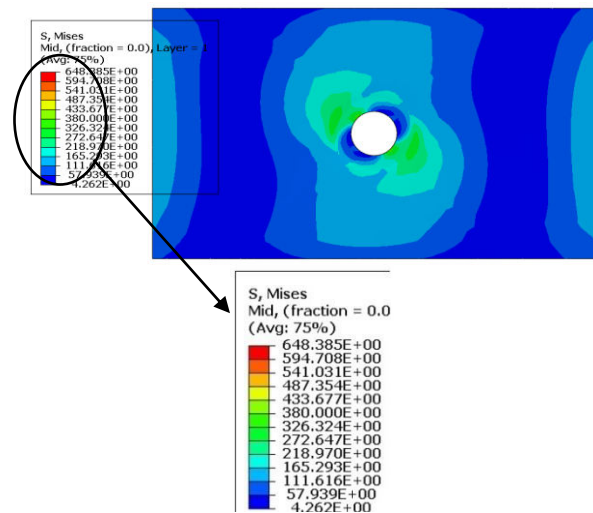


(c) With a solid shim

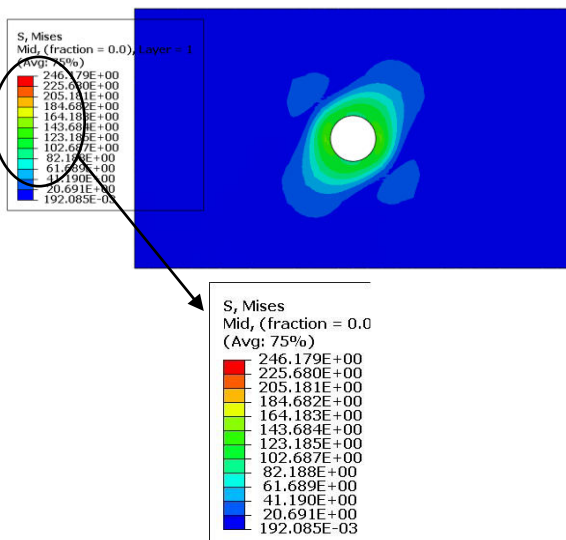
Figure-41. Stress distribution for an assembly gap of 0.3mm.**Figure-42.** Stress distribution for an assembly gap of 0.5mm.



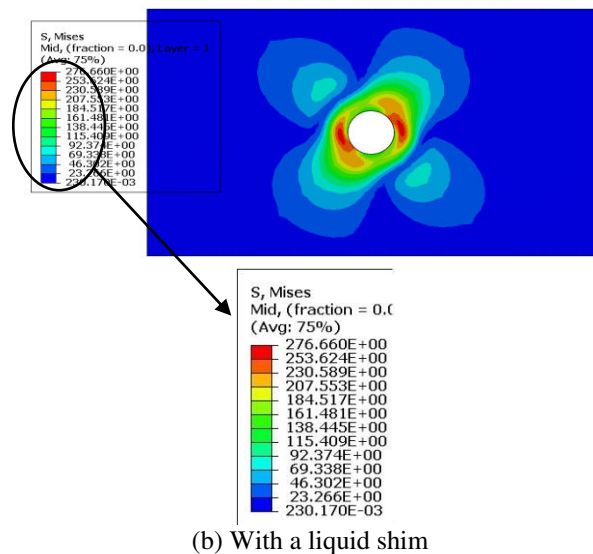
(a) Without any shim material



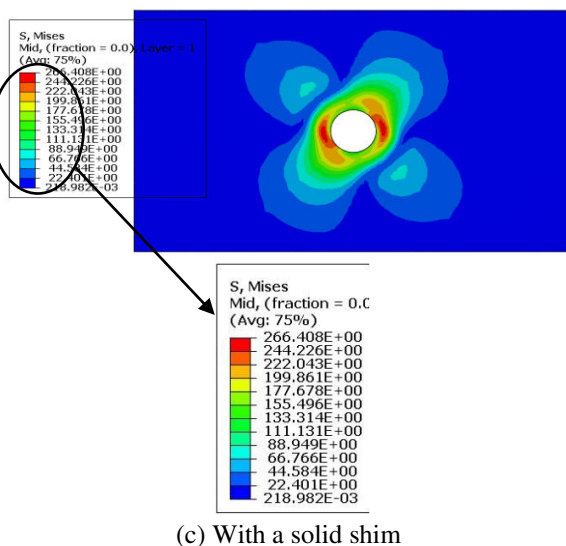
(a) Without any shim material



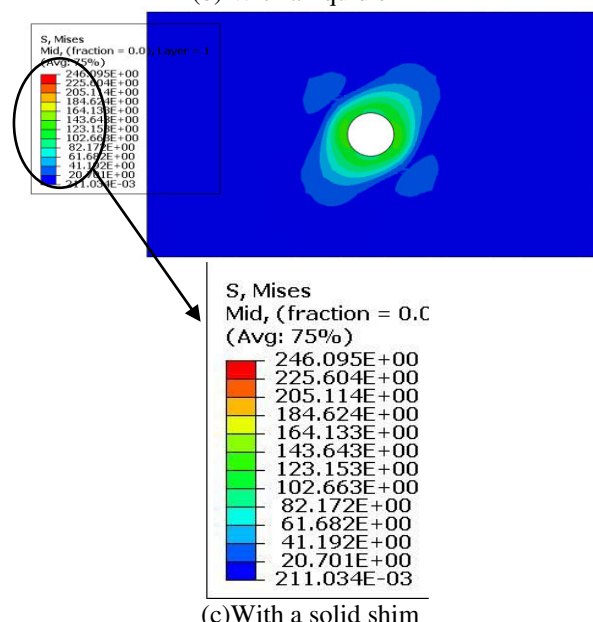
(b) With a liquid shim



(b) With a liquid shim



(c) With a solid shim



(c) With a solid shim

Figure-43. Stress distribution for an assembly gap of 0.7mm.**Figure-44.** Stress distribution for an assembly gap of 0.9mm.



Composite-aluminum assembled structure

The contour plots of the Von Mises stresses (S , Mises) as shown in Figures (45), (46), (47), (48) and (49) is the upper surface (surface interacting with the shim materials) of the bottom plate (aluminum) for the various assembly gaps (0.1, 0.3, 0.5, 0.7 and 0.9) (all dimensions in mm).

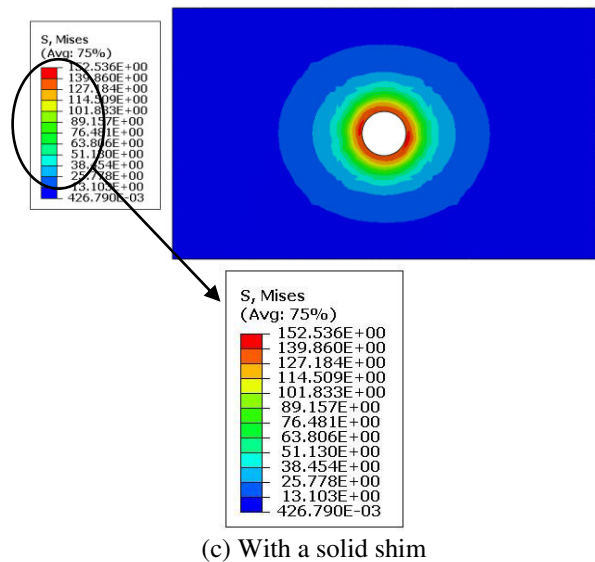
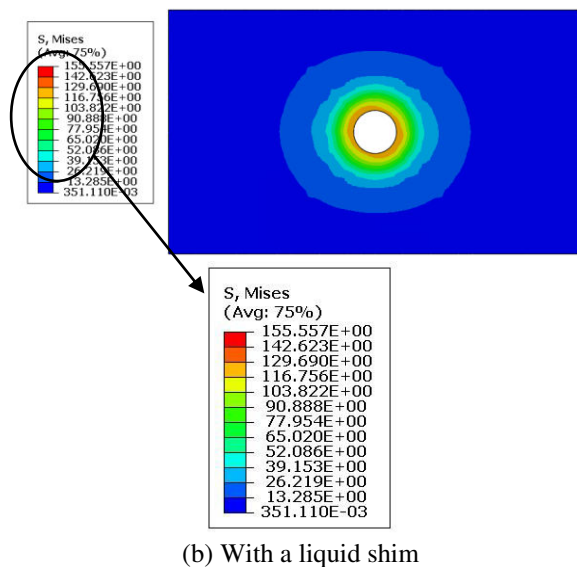
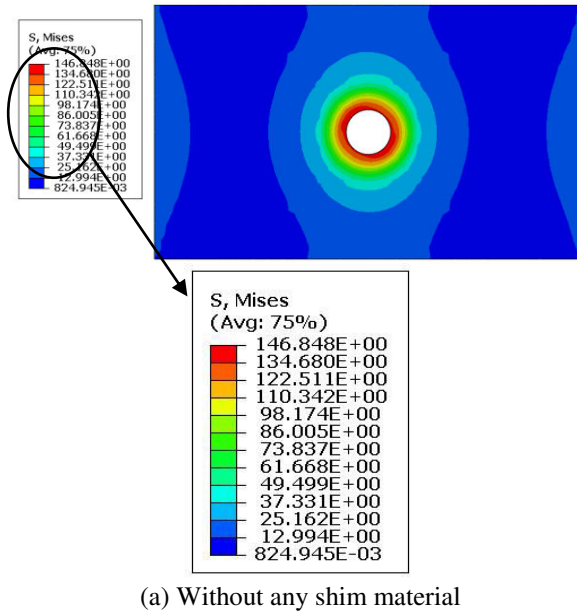
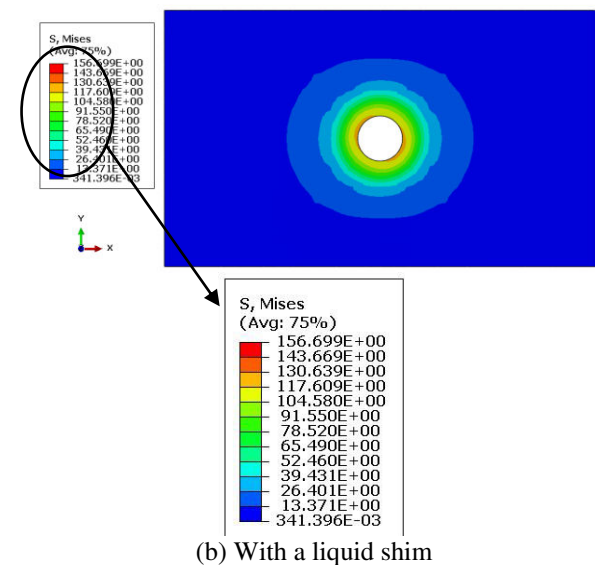
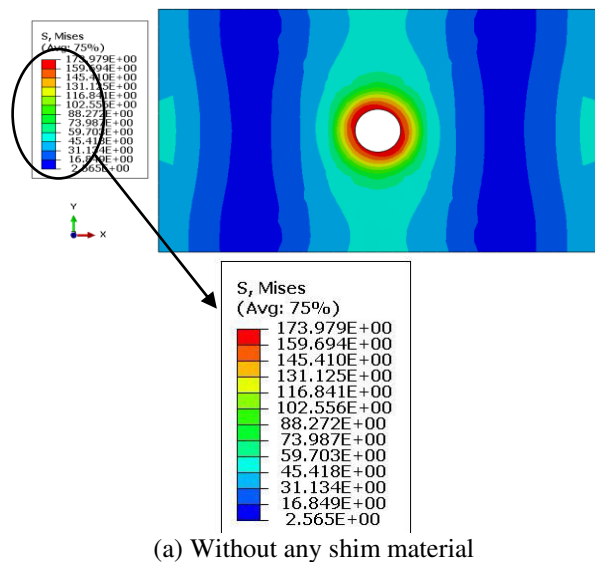
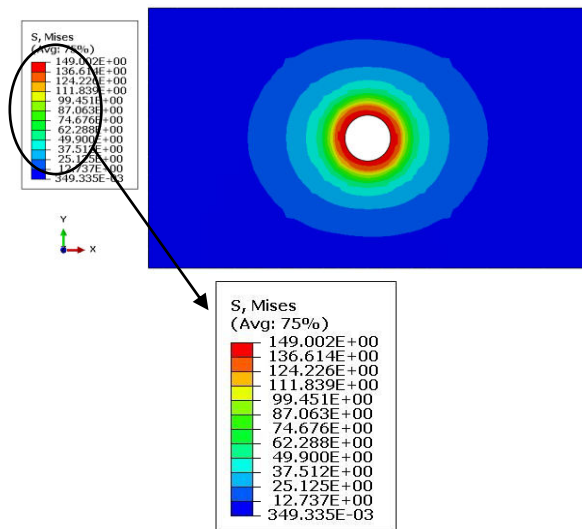


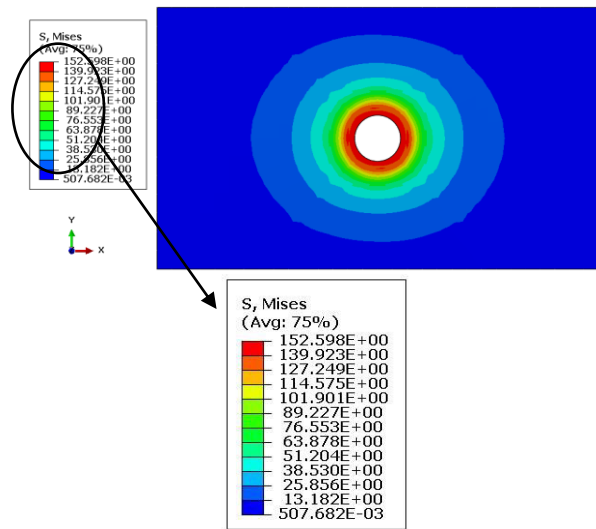
Figure-45. Stress distribution for an assembly gap of 0.1mm.





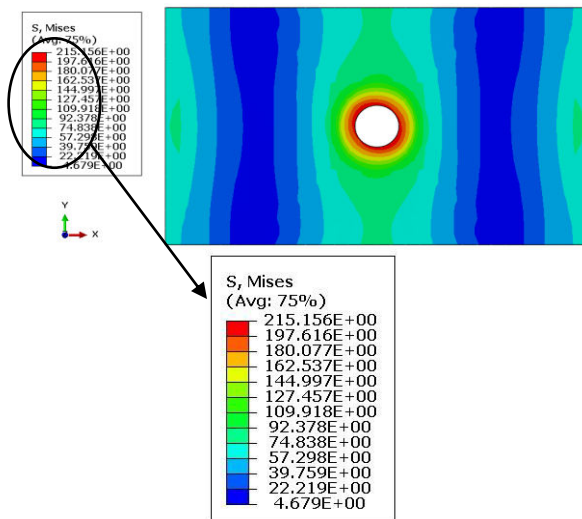
(c) With a solid shim

Figure-46. Stress distribution for an assembly gap of 0.3mm.

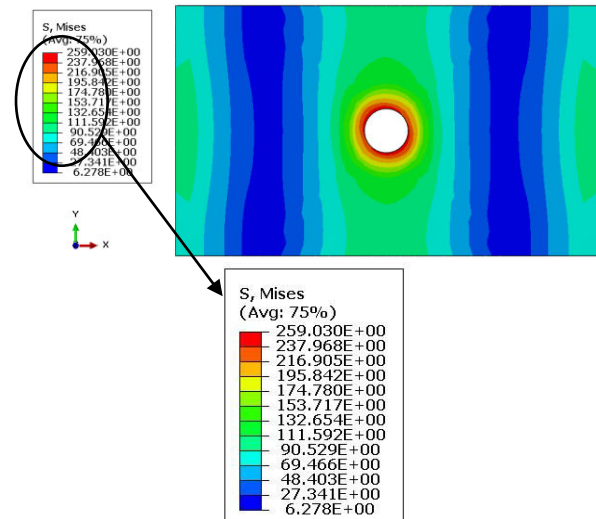


(c) With a solid shim

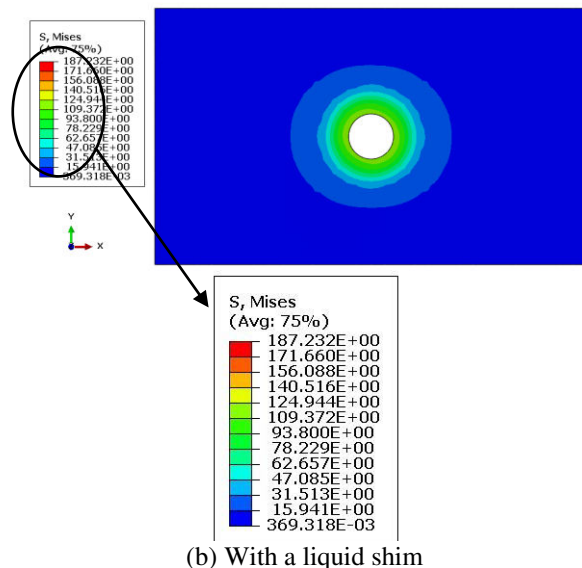
Figure-47. Stress distribution for an assembly gap of 0.5mm.



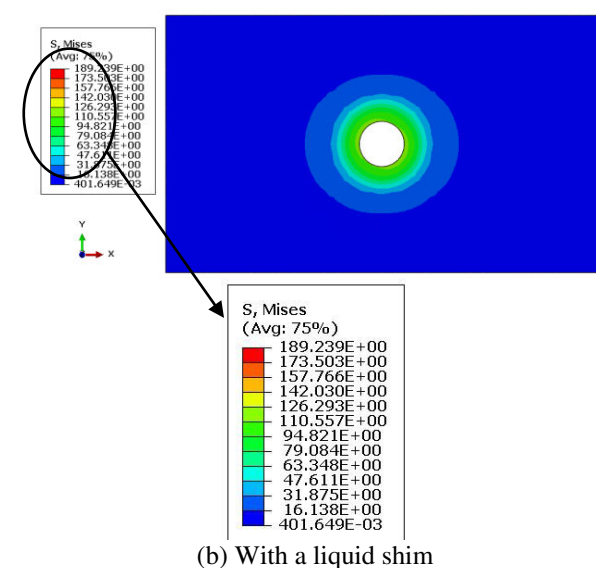
(a) Without any shim material



(a) Without any shim material



(b) With a liquid shim



(b) With a liquid shim

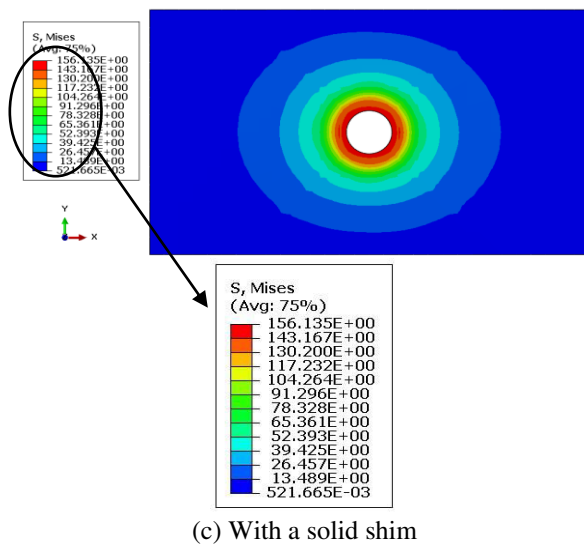


Figure-48. Stress distribution for an assembly gap of 0.7mm.

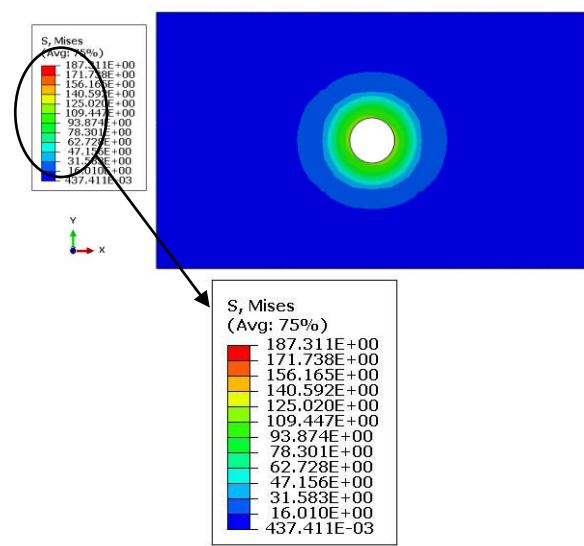
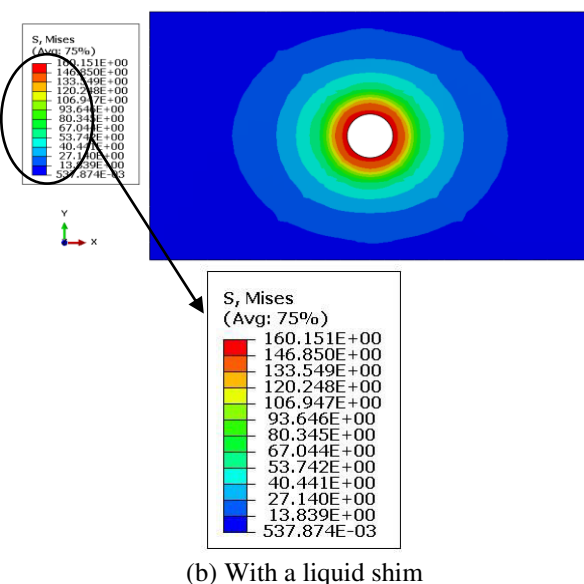
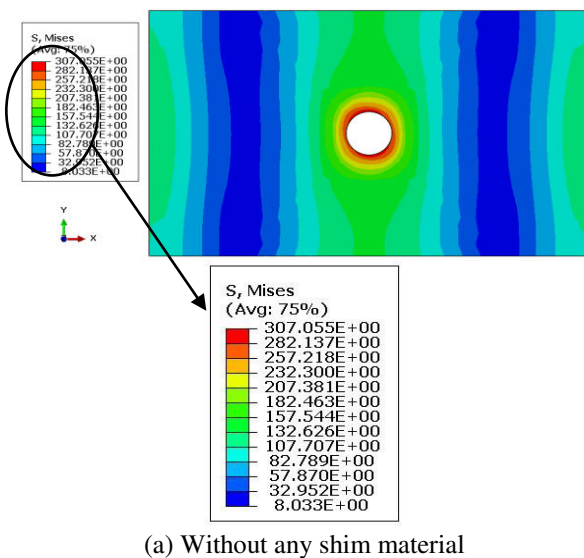


Figure-49. Stress distribution for an assembly gap of 0.9mm.



It is clear from Figures (40), (41), (42), (43), (44), (45), (46), (47), (48) and (49) that the stress distributions are greatly influenced by the assembly gaps with maximum concentrations being at the hole. In the case of the influence of shim materials, it is observed that the shims significantly reduced the stress distributions with the reductions showing that: (1) liquid shims were better fit for the assembly gaps 0.1mm, 0.3mm, 0.5mm and 0.7mm, and (2) solid shims were better fit for an assembly gap of 0.9mm. The trends observed for the stress distributions for Figures (40), (41), (42), (43), (44), (45), (46), (47), (48) and (49) were same as the ones depicted by Figures (30), (31), (32), (33), (34), (35), (36), (37), (39) and (39).

CONCLUSIONS

The influence of the assembly gap and shims on the strains and stresses of a bolted composite-aluminum structure was carried out using a three-dimensionally non-linear static analysis using the commercial finite element software ABAQUS. The trend observed was that, the strain and stress behaviors depicted by the assembled structure is well in-line with the current practice of shimming procedure in the aerospace industry but more study is needed to conclusively make this assertion since other factors such as the thermal expansion coefficients; failure and fracture mechanisms; and degree of plasticity might influence the trend observed in this paper for a composite-aluminum structure.

ACKNOWLEDGEMENT

The authors wish to acknowledge the Innovation Foundation of National Research Center for Commercial Aircraft Manufacturing Engineering Technology in China (SAMC13-JS-13-021) and Jiangsu Key Laboratory of Precision and Micro-Manufacturing Technology for the provision of financial support.



REFERENCES

- [1] Mallick P K. 2007. Fiber-Reinforced Composites: Materials, Manufacturing, and Design. 3rd edition. New York: CRC Press. pp. 1-12.
- [2] Vlot A, Gunnink JW. 2001. Fibre Metal Laminates. The Netherlands: Kluwer Academic Publishers, Dordrecht.
- [3] 2016. Materials breakdown of the Boeing 787. Available at: <http://science-in-news.blogspot.com/2012/09/carbon-fibre-a-new-era-in-aircraft-design.html> Date accessed 07/11/2016.
- [4] 2016. Eurofighter Typhoon. Available at: <http://www.eurofighter.com/downloads/TecGuide.pdf> Date accessed 07/11/2016.
- [5] Camponeschi ET, Bohlman R E, Hall J, *et al.* 1994. The Effect of Assembly Fit Up Gaps on the Compression Response of Thick Section Carbon/Epoxy Composites. ASTM STP 1185, Philadelphia. 137-138.
- [6] Dhôte J X, Comer A J, Stanley W F, *et al.* 2014. Investigation into compressive properties of liquid shim for aerospace bolted joints. Compos Struct. 109:224-230.
- [7] Smith J. 2011. Concept development of an automated shim cell for F-35 forward fuselage outer mold line control [MSc Thesis]. Menomonie: University of Wisconsin-Stout.
- [8] Lee R. 2016. Evaluation of shimming options with applications to JSF. Available at: <http://materialchemistry.com/DreamHC/Download/JSF%20Shimming%20Analysis.pdf>. Date accessed 21/03/2016.
- [9] Caracciolo P, Kuhlmann G. 2006. Reliability analysis in bolted composite joints with shimming material [Conference Proceedings] // 25th international congress of the aeronautical sciences. Hamburg, Germany: Paper 524.
- [10] Hühne C, Zerbst A K, Kuhlmann G, *et al.* 2010. Progressive damage analysis of composite bolted joints with liquid shim layers using constant and continuous degradation models. Compos Struct. 92(2):189-200.
- [11] Dhôte J X, Comer A J, Stanley W F, *et al.* 2013. Study of the effect of liquid shim on single-lap joint using 3D Digital Image Correlation. Compos Struct. 96: 216-225.
- [12] Comer AJ, Dhôte JX, Stanley WF, *et al.* 2012. Thermo-mechanical fatigue analysis of liquid shim in mechanically fastened hybrid joints for aerospace applications. Compos Struct. 94(7): 2181-2187.
- [13] Liu L. 2014. The influence of the substrate's stiffness on the liquid shim effect in composite to titanium hybrid bolted joints. Proc IMechE, Part G: J Aerospace Engineering. 228(3):470-479.
- [14] Zhai Y, Li D, Li X, *et al.* 2015. An experimental study on the effect of joining interface condition on bearing response of single-lap, countersunk composite-aluminum bolted joints. Compos Struct. 134:190-198.
- [15] Zhang G. 2015. Research on Assembly Gap Compensation for Aircraft Composite Components [MSc Thesis]. Nanjing: Nanjing University of Aeronautics and Astronautics:19-20.
- [16] Henkel Hysol EA 9394. Technical data sheet. Rev. 6/02.
- [17] Zhao T W, Zhang J X, Jiang Y. 2008. A study of fatigue crack growth of 7075-T651 aluminum alloy. Int J Fatigue. 30(7):1169-1180.
- [18] Mahoney M W, Rhodes C G, Flintoff J G, *et al.* 1998. Properties of friction-stir-welded 7075-T651 aluminum. Metall and Mat Trans A. 29(7):1955-1964.
- [19] 2013. ASTM Standard D5961/D 5961M-13, Standard test method for bearing response of polymer matrix composite laminates. West Conshohocken, PA, USA: ASTM International.
- [20] 2007. ASTM Standard D5766/D5766M-07, Standard test method for open-hole tensile strength of polymer matrix composite laminates. West Conshohocken, PA, USA: ASTM International.
- [21] 2013. ABAQUS. Inc. ABAQUS version 6.13 Documentation. Dassault Systemes/SIMULIA.
- [22] De Luca, Caputo F, Lamanna G, *et al.* 2013. Study of analytical models for predicting impact damage to composite structures [Conference Proceedings] // Italian Association for Stress Analysis 42nd National Congress. Salerno, Italy: University of Salerno. 11-14. (in Italian)



- [23] Zhao TW, Jiang Y. 2008. Fatigue of 7075-T651 aluminum alloy. *Int J Fatigue*. 30(5):834-849.
- [24] Kapidzic Z, Nilsson L, Ansell H. 2014. Finite element modeling of mechanically fastened composite-aluminum joints in aircraft structures. *Compos Struct*. 109:198-210.
- [25] Zhai Y, Li D, Li X, *et al.* 2015. An experimental study on the effect of bolt-hole clearance and bolt torque on single-lap, countersunk composite joints. *Compos Struct*. 127:411-419.
- [26] Sun C T. 2014. Adhesively Bonded Joints, Part 1: Bondline Thickness Effects and Hybrid Design of Adhesively Bonded Joints. DOT/FAA/AR-11/1, P1, USA: FAA report.
- [27] Hartman D R, Greenwood M E, Miller D M. 2006. High Strength Glass Fibers. Owens Corning Inc., Technical paper ref. 1-PI-19025-A, July 1996. Reprinted by AGY LLC as Pub. No. LIT-2006-111 (02/06).
- [28] Stocchi C, Robinson P, Pinho S T. 2013. A detailed finite element investigation of composite bolted joints with countersunk fasteners. *Compos Struct: Part A*. 52:143-150.
- [29] Chakherlou T N, Oskouei R H, Vogwell J. 2008. Experimental and numerical investigation of the effect of clamping force on the fatigue behaviour of bolted plates. *Eng Fail Anal*. 15(5):563-574.
- [30] Ekh J, Schon J, Melin L G. 2005. Secondary bending in multi fastener, composite-to-aluminium single shear lap joints. *Compos Struct: Part B*. 36(3):195-208.